A Cascaded Multilevel Modular Energy Router Hybrid Photovoltaic and Energy Storage With Improved Power Balance Capability

Xiaofeng Sun, *Member, IEEE*, Xinlei Liu, Jiaxun Teng, *Student Member, IEEE*, Ying Zhang, Lei Qi, Wei Zhao, and Xin Li

***Abstract*—Cascaded H-bridge (CHB) converter has become an attractive topology for future large-scale photovoltaic (PV) plants in medium-voltage microgrids. However, the unequal irradiation and aging degree of PV arrays will lead to imbalanced and inconsistent output power between the three phases. This article presents a novel approach to integrating PV and energy storage (ES) systems inherent in microgrids, utilizing a hybrid CHB-based energy router (HCHB-ER), which is configured with a limited number of submodules to connect with the centralized ES. The proposed topology can handle serious interphase power imbalance and respond to grid-side power scheduling, without the appearance of overmodulation and common-mode voltage rise caused by traditional zero-sequence voltage injection methods. Under the three major constraints from the modulation level, the centralized energy storage maximum intrapower regulation boundary and submodule configuration ratio are analyzed in detail. Additionally, the power imbalance regulation capability of the proposed HCHB-ER across various configuration ratios is thoroughly evaluated and compared with the zero-sequence injection methods. Finally, the correctness and effectiveness of the proposed strategy are verified by simulations and experiments.**

***Index Terms*—Cascade H-bridge (CHB), centralized energy storage (CES), interphase power imbalance, photovoltaic (PV).**

I. Introduction

With the advantages of no noise, no pollution, and low emissions, photovoltaic (PV) systems are considered to be the clean energy with the fastest-growing installed capacity in many microgrid systems around the world [1], [2], [3]. A typical medium-voltage dc distribution network is shown in Fig. 1 [2], [3], [4]. The PV inverter is the core part of the PV energy conversion system, which integrates the dc into the medium-voltage ac grid.

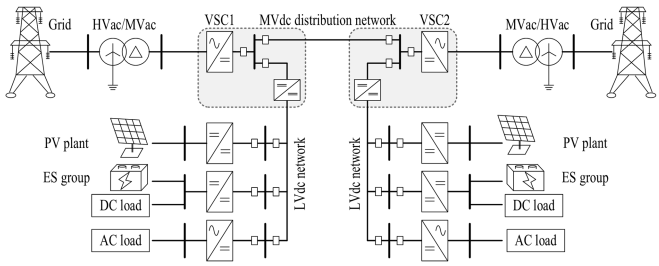

Fig. 1. Typical medium-voltage DC distribution network [2], [3], [4].

Compared to traditional two-level converters, multilevel converters exhibit better performance, making them more suitable for medium-voltage conversion applications [5]. The cascaded H-bridge (CHB) topology presents an appealing solution for future large-scale PV plants due to its modular structure and each submodule (SM) ability to achieve independent maximum power point tracking (MPPT), which is particularly suitable for distributed PV access and direct connection to medium-voltage grids. The CHB converter is divided into star and delta configurations. Star configuration has fewer converter-cell counts and the lowest cost, which is more suitable for utility applications [6]. Therefore, the star configuration is chosen as the research topology in this article.

A. State-of-the-Art Power Imbalance Methods

Fig. 2 shows the traditional three-phase CHB-based PV (CHB-PV) converters. The interconnection of the PV and SMs can be divided into two types: nonisolated and isolated. Since the insulation withstand capability of commercial PV panels is below 1500 V, the isolated CHB-PV converter is better suited for medium-voltage and high-power applications, whereas the nonisolated CHB-PV converter is currently more appropriate for single-phase, lower-power applications [7]. The three-phase isolated CHB-PV has been extensively investigated in numerous articles, with research topics mainly including topologies [8], [9], reactive power compensation [10], fault ride-through [11], [12], modulation strategies [13], [14], and so on.

Manuscript received 26 June 2023; revised 17 September 2023; accepted 20 October 2023. Date of publication 26 October 2023; date of current version 26 January 2024. This work was supported in part by the National Natural Science Foundation of Hebei Province under Grant E2021203162 and in part by the Key Research and Development Program of Hebei Province under Grant 19214405D. Recommended for publication by Associate Editor M. ElMoursi. *(Corresponding authors: Jiaxun Teng; Xin Li.)*

The authors are with the Key Laboratory of Power Electronics for Energy Conversion and Motor Drive of Hebei Province, Department of Electronics Engineering, Yanshan University, Qinhuangdao 066004, China (e-mail: sxf@ysu.edu.cn; liuxinlei@stumail.ysu.edu.cn; tengjiaxun@stumail.ysu.edu.cn; ysudyzy@ysu.edu.cn; qil@ysu.edu.cn; zwysu@ysu.edu.cn; yddylixin@ysu.edu.cn).

Color versions of one or more figures in this article are available at https://doi.org/10.1109/TPEL.2023.3327684.

Digital Object Identifier 10.1109/TPEL.2023.3327684

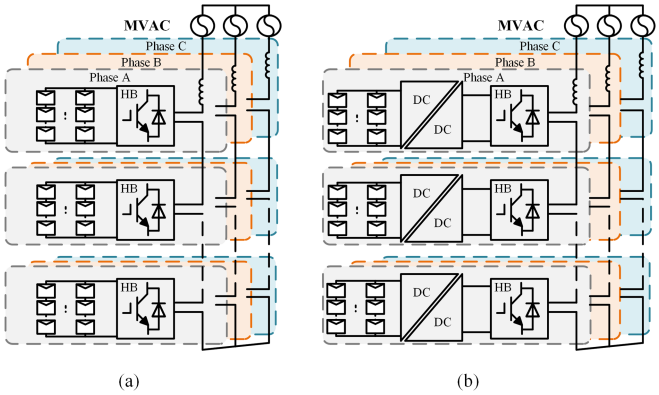

Fig. 2. Traditional three-phase CHB-PV converter. (a) Nonisolated. (b) Isolated.

However, a common challenge in the three-phase CHB-PV system is the unequal output power of each H-bridge due to nonuniform solar irradiance and varying ambient temperature across PV panels. This leads to intermodule power imbalance and interphase power imbalance [7], [8], [9], [10], [11], [12], [13], [14]. While the issue of intermodule power imbalance has been analyzed in many single-phase CHB systems [15], [16], this research focuses on addressing interphase power imbalance. For the elimination strategy of interphase power imbalance in CHB converter, it can be mainly divided into two types of methods, which are voltage injection methods and optimal configuration methods.

The first type is to inject a zero-sequence voltage into three-phase CHB-stage [17], [18], [19], [20], [21], [22], [23], [24], [25]. In [17], the fundamental frequency zero-sequence voltage (FFZSI) was first injected into the output voltage of the CHB-stage, which solves the problem of grid-connected current asymmetry caused by the unbalance of PV output power between phases. However, the FFZSI can easily cause overmodulation of the CHB converter output voltage, which should be less than the sum of the CHB dc-side voltages. Therefore, the FFZSI has poor interphase power balancing capability. In order to extend the power balance capability of FFZSI, Yu et al. in [18], [19], [20], and [21] introduced high-order harmonic components with specific frequencies into the system. As third harmonic injection (THI) can significantly improve the dc-side voltage utilization, the THI has been proposed in [18] to extend the range of interphase power balancing capabilities. On this basis, three kinds of THI methods are proposed in [19]. Among them, the double min–max zero-sequence voltage injection has the best power balance capabilities, but it still does not achieve the maximum utilization of dc-side voltage of the converter. An optimal zero-sequence voltage injection (OZSI) method based on the iterative method was proposed in [20], which has fast convergence and is well-suited for digital control implementation. To compare the power balancing capability of various zero-sequence voltage injection methods mentioned above, an index coefficient power balance factor (PBF) and three-dimensional (3-D) graph power balance space (PBS) have been defined in [21]. The results of the study show that compared to other injection methods, FFZSI has the worst balancing capability. Although simplified OZSI exhibits superior power balancing capability across all injection methods, it may result in network pollution by introducing negative-sequence components of the grid current. In addition, these methods of harmonic injection and power balance capability analysis are also suitable for extending and analyzing the single-phase CHB intermodule power balance region [16].

The second type is the improved configuration methods, which is usually achieved by changing the topology connection, adding additional magnetic elements and circuits, etc. In [22] and [23], the working principle and control implementation of the delta-connected CHB-PV converter were discussed and concluded that the delta-connected CHB-PV converter greatly improves the power balancing capability combining injection methods compared with the star-connected CHB-PV converter. A three-phase CHB-PV topology based on common dc bus was proposed in [24]. The problem of intermodule and interphase power imbalance is avoided by establishing a common dc bus channel, but this type of topology usually uses a three-stage structure, which increases power losses and affects the overall efficiency of the system [7].

In summary, for the first type of methods: the injection of high-order harmonic components in FFZSI improves the power balancing capability, but the high-order harmonic will increase the system common-mode voltage of the system, which causes harm to the network side and power devices [25]. For the second type of methods: the change of the topology configuration may improve the interphase power balancing capability, but this method increases the complexity of the system and configuration [22], [23], [24]. Furthermore, the above two types of methods have a common problem. Due to the influence of uncontrollable factors such as climate change, the grid-connected power of the converter varies with the PV output power, resulting in a reduction of system rotational inertia [26].

Recently, hybrid systems that combine energy storage (ES) and PV have attracted much attention. The flexibility of ES makes up for the intermittency of PV system power generation [27], [28], [29], [30], [31], which improves the efficiency and reliability of PV power generation. The simultaneous configuration of PV and ES in each SM is proposed in [29] and [30], and the power balancing is achieved using the cooperative operation of PV and ES. However, it is difficult to balance the state-of-charge (SOC) of ES between different SMs. In practical engineering, the assembly of multiple groups of ES is both costly and challenging. The stabilizing unit, where the battery and each phase are connected via dc–dc converters, was proposed in [31] to balance the PV output imbalance power. However, the power balance mechanism associated with the conditions of stable system operation is not clear, and the number of stabilizing unit constraints is not explained.

B. Typical Medium-Voltage Energy Router Demonstration Projects

Table I presents the compilation of typical microgrid demonstration projects worldwide [33], [34], [35], [36]. In the Zhangbei New energy microgrid demonstration project, the PV output

TABLE I
COMPILATION OF TYPICAL MICROGRID DEMONSTRATION PROJECTS WORLDWIDE [33], [34], [35], [36]

Project name	Voltage level	PV power	ES power	ES capacity
Zhangbei, China [33]	35 kV	40 MW	10 MW	10 MWh
Yanqing, China [33]	10 kV	25 MW	12.4 MW	//
Hefei, China [33]	10 kV	4.1 MW	2 MW	4 MWh
Haidian, China [33]	10 kV	50 MW	5 MW	10 MWh
Shanxi, China [33]	10 kV	20 MW	2 MW	4 MWh
Hachinohe, Japan [34]	//	80 MW	100 MW	660 kWh
Kythnos, Greece [35]	400 V	10 kW	//	53 kWh
DeMoTec, German [36]	//	2 kW	10 kW	//

power is 40 MW, the configured ES power is 12.4 MW, and the voltage level is 35 kV. In the Beijing Haidian New energy microgrid demonstration project, the rooftop PV output power is 50 MW, the configured ES power is 5 MW, the capacity is 10 MWh, and it is connected to the 10 kV distribution network. As can be seen from the above practical engineering examples, as a flexible power regulation resource, ES is usually equipped with additional ES and conversion components in a PV area to make up for the randomness of new energy generation and improve the grid reliability [37], [38].

C. Contribution

In this article, the ES and PV systems configured in one microgrid are integrated into the same conversion device, and a hybrid CHB-based energy router (HCHB-ER) is proposed, in which a small number of SMs configure in the CHB-PV system interconnected with centralized energy storage (CES). This article intends to contribute in the following aspects.

1) The proposed topology eliminates the interphase power imbalance by adjusting the configured ES module power, which can handle serious unbalanced conditions and respond to the grid-side power scheduling.
2) Under the three major constraints from the modulation level, the intrapower regulation boundary and ES SM configuration ratio are analyzed in detail, which provides a security domain for the hybrid configuration stable operation.
3) Compared with the distributed ES separately configured in each PV-SM, this hybrid configuration topology reduces the number of components and avoids the problem of balancing the SOC for the distributed energy system.

The rest of this article is organized as follows. In Section II, the mathematical model of the three-phase CHB-PV converter is established to analyze the interphase power imbalance mechanisms and review the existing zero-sequence voltage injection methods. In Section III, the HCHB-ER is proposed. Then, the proposed topology is compared with the existing zero-sequence voltage injection methods and other ES schemes in Section IV. Simulation and experiment verify the ability of the proposed topology to handle interphase imbalance power under different configurations in Sections V and VI. Finally, Section VII concludes the article.

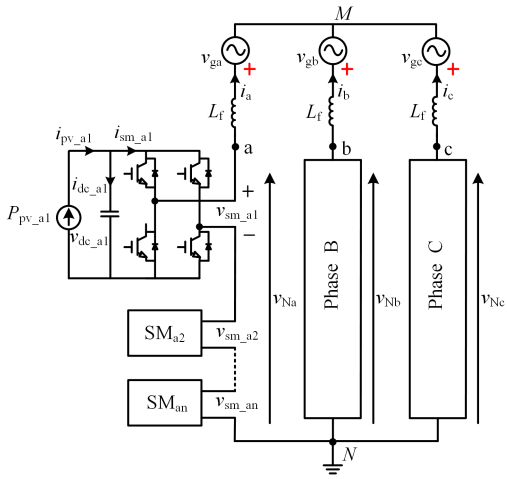

Fig. 3. Equivalent model of three-phase isolated CHB-PV converter.

II. POWER IMBALANCE ANALYSIS AND INJECTION METHODS OF TRADITIONAL THREE-PHASE CHB-PV CONVERTER

A. Mathematical Model

The equivalent model of the three-phase isolated CHB-PV converter is shown in Fig. 3, each phase of which is formed by n SMs and one filter inductance. The dc–dc converter shown in Fig. 2(b) provides current isolation between PV panels and SMs, and provides independent MPPT control for each distributed PV module, which realizes the decoupling control of the PV system and the CHB converter. Therefore, distributed PV modules and isolated dc–dc converters can be equivalent to power current sources connected to SMs [32].

In Fig. 3, v_{gx} and i_x are the ac side voltage and current, respectively, whereas v_{Nx} represents the converter output voltage of phase-x (x represents a, b, and c); i_{pv_xi} and P_{pv_xi} are the PV current and power injected into the SM of phase-x, respectively; i_{sm_xi} and v_{sm_xi} are the SM outputs current and voltage, respectively; i_{dc_xi} and v_{dc_xi} are the SM capacitance current and voltage, respectively; and L_f is the filter inductance.

When the PV panel injects the same power into each SM, taking phase-a as an example, the switching function of the ith SM is as follows:

$$F_{ai} = \frac{v_{sm\_ai}}{v_{dc\_ai}} \tag{1}$$

and the output voltage of three-phase converter can be obtained as

$$\begin{cases} v_{Na} = \sum_{i=1}^{n} v_{dc\_ai} F_{ai} \\ v_{Nb} = \sum_{i=1}^{n} v_{dc\_bi} F_{bi} \\ v_{Nc} = \sum_{i=1}^{n} v_{dc\_ci} F_{ci}. \end{cases} \tag{2}$$

According to the KVL theorem, the CHB-PV voltage loop equation can be derived in (3), and the equivalent circuit model of the three-phase CHB-PV converter can be established, as shown

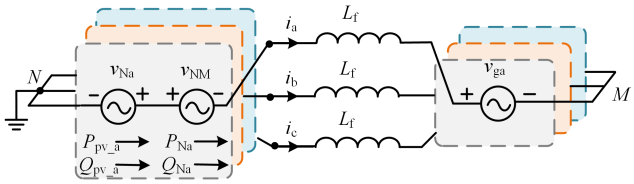

Fig. 4. Equivalent circuit model of three-phase CHB-PV converter.

in Fig. 4

$$\begin{cases} v_{\mathrm{Na}} = L_{\mathrm{f}} \frac{di_{\mathrm{a}}}{dt} + v_{\mathrm{ga}} + v_{\mathrm{NM}} \\ v_{\mathrm{Nb}} = L_{\mathrm{f}} \frac{di_{\mathrm{b}}}{dt} + v_{\mathrm{gb}} + v_{\mathrm{NM}} \\ v_{\mathrm{Nc}} = L_{\mathrm{f}} \frac{di_{\mathrm{c}}}{dt} + v_{\mathrm{gc}} + v_{\mathrm{NM}} \end{cases} \tag{3}$$

where v_{NM} is the common-mode voltage between ground and the neutral point of the inverter.

B. Analysis of Interphase Power Imbalance

The focus of this section is to analyze the power imbalance between the phases of the CHB converter, so it is assumed that the output power of each SM in the same phase is uniform, that is, $P_{\mathrm{pv\_x1}} = P_{\mathrm{pv\_x2}} = \ldots\ldots = P_{\mathrm{pv\_xn}}$, whereas the output power of each phase is not uniform, that is, $P_{\mathrm{pv\_a}} \neq P_{\mathrm{pv\_b}} \neq P_{\mathrm{pv\_c}}$. In order to intuitively reflect the degree of power imbalance between phase, l_{x} (x = a, b, c) is defined as the PV generation power coefficient of each phase

$$l_{\mathrm{x}} = \frac{P_{\mathrm{pv\_x}}}{P_{\mathrm{N}}/3} \tag{4}$$

where $P_{\mathrm{pv\_x}}$ (x represents a, b, and c) is the PV instantaneous power of each phase; and P_{N} is the rated output power of CHB converter.

According to (3), the power conservation expression between the converter and the grid side can be derived as

$$\begin{cases} P_{\mathrm{pv\_a}} = v_{\mathrm{Na}} i_{\mathrm{a}} = L_{\mathrm{f}} \frac{di_{\mathrm{a}}}{dt} i_{\mathrm{a}} + v_{\mathrm{ga}} i_{\mathrm{a}} + v_{\mathrm{NM}} i_{\mathrm{a}} \\ P_{\mathrm{pv\_b}} = v_{\mathrm{Nb}} i_{\mathrm{b}} = L_{\mathrm{f}} \frac{di_{\mathrm{b}}}{dt} i_{\mathrm{b}} + v_{\mathrm{gb}} i_{\mathrm{b}} + v_{\mathrm{NM}} i_{\mathrm{b}} \\ P_{\mathrm{pv\_c}} = v_{\mathrm{Nc}} i_{\mathrm{c}} = L_{\mathrm{f}} \frac{di_{\mathrm{c}}}{dt} i_{\mathrm{c}} + v_{\mathrm{gc}} i_{\mathrm{c}} + v_{\mathrm{NM}} i_{\mathrm{c}}. \end{cases} \tag{5}$$

Combined with (5), the output power of each phase is equal to the product of the output voltage of the converter and the grid side current. When the PV output power between the phases of the converter is unequal ($l_{\mathrm{a}} \neq l_{\mathrm{b}} \neq l_{\mathrm{c}}$) and the output voltage of the converter does not change, the three-phase grid current will be asymmetry, as shown in Fig. 5 [17]. To clarify the meaning of the various symbols, the vector symbols are shown in bold, where $\boldsymbol{V}_{\mathrm{ga}}, \boldsymbol{V}_{\mathrm{gb}}, \boldsymbol{V}_{\mathrm{gc}}$ and $\boldsymbol{I}_{\mathrm{a}}, \boldsymbol{I}_{\mathrm{b}}, \boldsymbol{I}_{\mathrm{c}}$ represent the grid voltage and current vectors, respectively; $\boldsymbol{V}_{\mathrm{L}}$ represents the voltage vectors of the filter inductance; and $\boldsymbol{V}_{\mathrm{Na}}$, $\boldsymbol{V}_{\mathrm{Nb}}$, and $\boldsymbol{V}_{\mathrm{Nc}}$ represent the output voltage vectors of the converter, respectively.

C. State-of-the-Art Zero-Sequence Voltage Injection Methods

According to (3) and (5), the common-mode voltage component v_{NM} exists in three phases. Therefore, the zero-sequence voltage injection strategy balances the difference between the output power of three-phase CHB-PV by changing the common-mode voltage component v_{NM}. In addition, due to the symmetry of the three-phase grid current, the injected zero-sequence voltage does not generate additional active power.

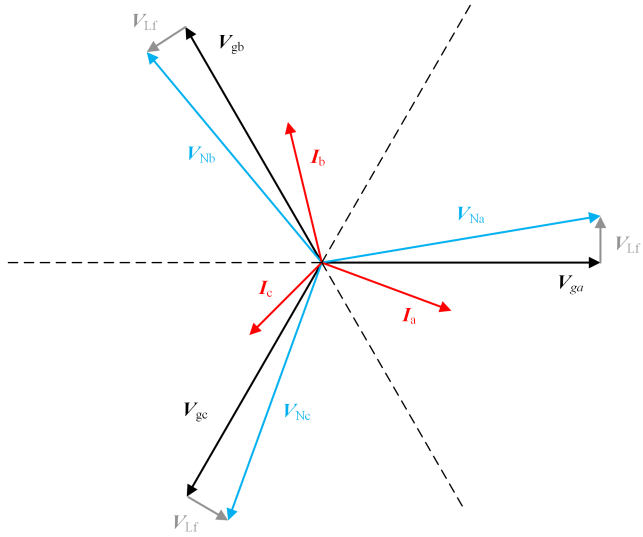

Fig. 5. Three-phase diagram for interphase imbalance operation of CHB-PV converter.

1) Fundamental Frequency Zero-Sequence Injection: When the output power of the three-phase is equal, the most common and basic injection method is to inject the FFZSI. The FFZSI expression has been derived in [17], [18], [19]

$$v_{\mathrm{FF}}^{0} = \sqrt{2} V^{0} \cos(\omega t + \xi) \tag{6}$$

where

$$V^{0} = \frac{\sqrt{2}}{(l_{\mathrm{a}} + l_{\mathrm{b}} + l_{\mathrm{c}})} V_{\mathrm{g}} \tag{7}$$

$$\xi = \begin{cases} \sin^{-1}\left(\frac{\sqrt{6}(l_{\mathrm{c}} - l_{\mathrm{b}})}{2\sigma}\right) & \mathrm{Sector(I),\ (VI)} \\ \frac{2\pi}{3} + \sin^{-1}\left(\frac{\sqrt{6}(l_{\mathrm{b}} - l_{\mathrm{a}})}{2\sigma}\right) & \mathrm{Sector(II),\ (III)} \\ \frac{4\pi}{3} + \sin^{-1}\left(\frac{\sqrt{6}(l_{\mathrm{a}} - l_{\mathrm{c}})}{2\sigma}\right) & \mathrm{Sector(IV),\ (V)} \end{cases} \tag{8}$$

$$\sigma = \sqrt{(l_{\mathrm{a}} - l_{\mathrm{b}})^2 + (l_{\mathrm{b}} - l_{\mathrm{c}})^2 + (l_{\mathrm{c}} - l_{\mathrm{a}})^2} \tag{9}$$

where V_0 represents the amplitude of the zero-sequence voltage, ξ represents the phase angle of zero-sequence voltage, and V_{g} represents the rms value of grid phase voltage. After the injection of the fundamental zero-sequence voltage, the converter output voltage of the phase-a can be expressed as follows:

$$\begin{aligned} v_{\mathrm{Na}} &= v_{\mathrm{Na}}^{+} + v_{\mathrm{FF}}^{0} \\ &= \sqrt{2} V_{\mathrm{cp}} \cos(\omega t + \varphi) + \sqrt{2} V^{0} \cos(\omega t + \xi) \end{aligned} \tag{10}$$

where $v^{+}{}_{\mathrm{Na}}$ represents the positive-sequence of the converter output voltage in phase-a, and V_{cp} and φ are the rms value and the power factor angle of the converter output positive-sequence voltage, respectively.

Fig. 6 shows that the phase diagram for interphase imbalance operation after FFZSI [18], where $\boldsymbol{V}^{\circ}{}_{\mathrm{FF}}$ represents the voltage

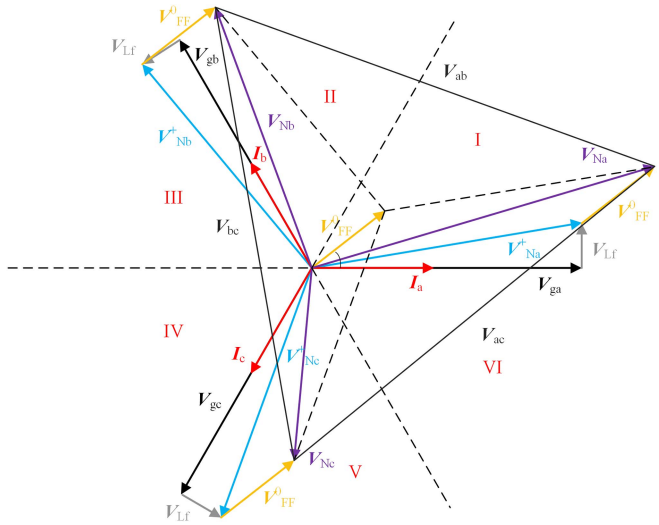

Fig. 6. Three-phase diagram for interphase imbalance operation after FFZSI [18].

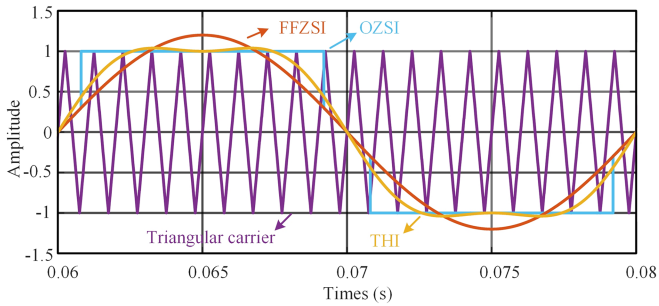

Fig. 7. Modulation waveforms for the three zero-sequence voltage injection methods.

vector of FFZSI; $\boldsymbol{V}^{+}{}_{\mathrm{Na}}$, $\boldsymbol{V}^{+}{}_{\mathrm{Nb}}$, and $\boldsymbol{V}^{+}{}_{\mathrm{Nc}}$ represent the converter output positive-sequence voltage vectors, respectively; $\boldsymbol{V}_{\mathrm{Na}}$, $\boldsymbol{V}_{\mathrm{Nb}}$, and $\boldsymbol{V}_{\mathrm{Nc}}$ represent the converter output voltage vectors after combining the positive and zero sequence components, respectively; and $\boldsymbol{V}_{\mathrm{ab}}$, $\boldsymbol{V}_{\mathrm{bc}}$, and $\boldsymbol{V}_{\mathrm{ac}}$ represent the converter output line-to-line voltage vectors after combining the positive and zero sequence components, respectively.

2) Harmonic Injection: The power balance capability of FFZSI is severely limited by the constraints on the dc-side voltage. Therefore, expanding the power balance capability of FFZSI can be translated into improving the dc-side voltage utilization.

The THI can effectively improve the dc-side voltage utilization, thus adding one-sixth third harmonic to the FFZSI can greatly reduce the output voltage peak of the converter output voltage and expand its power balance capability as shown in Fig. 7. Therefore, reduce third harmonic injection (RTHI) and double third harmonic injection (DTHI) have been derived in [19]. However, the THI still does not achieve the maximum utilization of dc-side voltage of the converter. OZSI has the best power balance capability in all zero-sequence injection methods

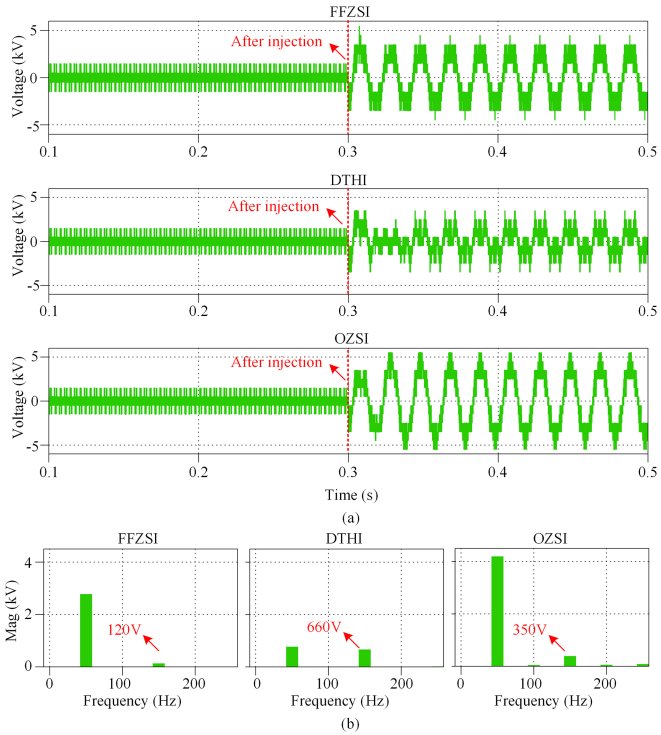

Fig. 8. Common-mode voltage (a) and FFT analysis (b) after injection.

[20]. As shown in Fig. 7, its core idea is to add a clamped signal to the zero-sequence voltage, clamping the overmodulation wave to a square wave signal.

Unfortunately, the OZSI has reached the limit of the converter output voltage and cannot be further expanded by any harmonic compensation. This method is very complex and needs to iterate repeatedly in the process of calculation, which takes up more computing resource of the control system [20]. In addition, and importantly, zero-sequence injection methods can balance the interphase power, but it increases the common-mode voltage of the system that has the influence on the switching devices and grid side, as shown in Fig. 8.

III. Proposed HCHB-ER With Improved Power Balance Capability

A. System Configuration

It should be noted that in typical demonstration projects, in order to make up for the intermittency of new energy power generation, PV will usually be equipped with ES, as shown in Section I-B. Therefore, in order to avoid the damage of the converter output voltage overmodulation and common-mode voltage change to the system caused by the zero-sequence injection, this article integrates the ES and PV into the same conversion device, and proposes the HCHB-ER, which eliminates the interphase power imbalance without changing the output voltage of the converter.

The configuration of the HCHB-ER is shown in Fig. 9, where each phase of the HCHB-ER consists of $n + m$ SMs. Among

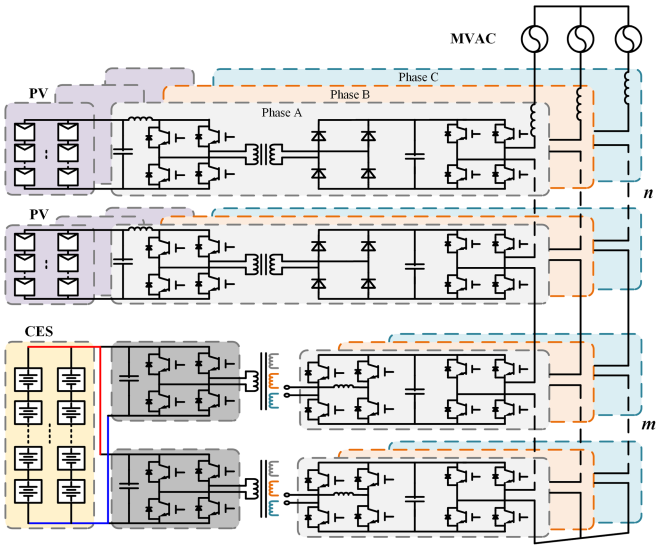

Fig. 9. Proposed HCHB-ER.

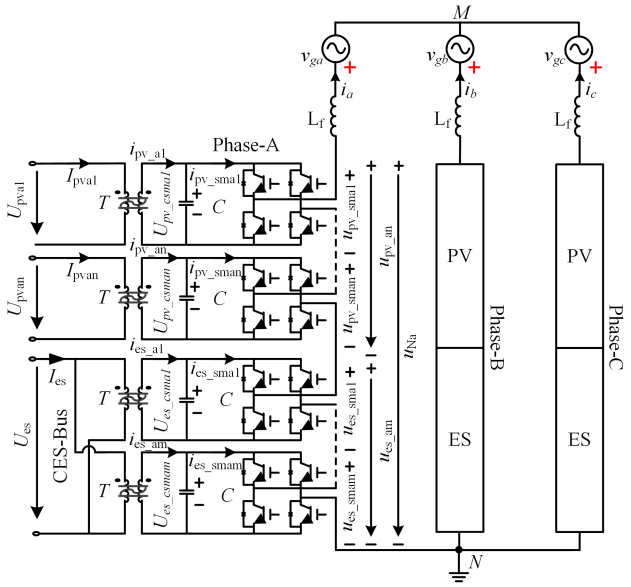

Fig. 10. Equivalent circuit model of HCHB-ER.

them, the number of n SMs is interconnected with PV panels through isolated boost converters, which provide current isolation for PV systems while realizing MPPT. The other m SMs are linked to the centralized ES via bidirectional isolated dc–dc converters, which employ quad-active-bridge (QAB) technology. When intraphase is configured with PV and ES, it can be defined that the SMs interconnected with PV are called PV-SMs, and the SMs interconnected with CES are called ES-SMs. The three-phase horizontal ES-SMs of CHB are cascaded with QAB, which reduces the cost and improves the power density of the system. On the primary of QAB, three active bridges transfer the energy power to the three-phase ES-SMs under the phase shift control strategy, and the secondary active bridge of QAB is connected to the CES dc-bus. The power provided by CES eliminates the unbalanced power generated by distributed PV among the CHB three-phase, enhances the stability of PV power generation, and satisfies the converter to output the rated power in response to the upper energy scheduling on the grid side.

B. Natural Power Balance Implementation by Central ES

The equivalent circuit model of the HCHB-ER is shown in Fig. 10, where u_{Na} is the converter output voltage of HCHB-ER; $u_{\mathrm{pv\_smai}}$, $u_{\mathrm{es\_smai}}$ and $i_{\mathrm{pv\_smai}}$, $\mathrm{i}_{\mathrm{es\_smai}}$ are the output voltages and currents of each PV-SM and ES-SM, respectively; $u_{\mathrm{pv\_an}}$ and $u_{\mathrm{es\_am}}$ are the sum of the output voltage of all PV-SMs and ES-SMs in phase-a, respectively; $U_{\mathrm{pv\_csmai}}$ and $U_{\mathrm{es\_csmaj}}$ are the PV-SM and ES-SM capacitor voltage of the phase-a, respectively; $i_{\mathrm{pv\_ai}}$ and $i_{\mathrm{es\_ai}}$ are the currents injected into the SM by the PV and CES through the dc–dc converter, respectively; T is the isolated dc–dc converter; and U_{pvai}, U_{es} and I_{pvai}, I_{es} are the input voltage and current of PV panel and CES on the input dc–dc converter side, respectively.

As shown in Fig. 10, PV-SMs and ES-SMs together constitute the output voltage of CHB converter after configuring the ES module. Therefore, taking phase-a as an example, the single-phase KVL equation can be written as follows:

$$\begin{cases} \boldsymbol{V}_{\mathrm{Na}} = \sum_{i=1}^{n} \boldsymbol{V}_{\mathrm{pv\_smai}} + \sum_{j=1}^{m} \boldsymbol{V}_{\mathrm{es\_smaj}} = j\omega L_f \boldsymbol{I}_a + \boldsymbol{V}_{\mathrm{ga}} \\ \sum_{i=1}^{n} \boldsymbol{V}_{\mathrm{pv\_smai}} = \sum_{i=1}^{n} \boldsymbol{S}_{\mathrm{pv\_ai}} U_{\mathrm{pv\_csmai}} \\ \sum_{j=1}^{n} \boldsymbol{V}_{\mathrm{es\_smaj}} = \sum_{j=1}^{n} \boldsymbol{S}_{\mathrm{es\_aj}} U_{\mathrm{es\_csmaj}} \end{cases} \tag{11}$$

where $\boldsymbol{V}_{\mathrm{Na}}$ is the converter output voltage vector, $\boldsymbol{S}_{\mathrm{pv\_ai}}$ and $\boldsymbol{S}_{\mathrm{es\_aj}}$ are the output voltage modulation ratio vectors of each PV-SM and ES-SM in phase-a, respectively, and $\boldsymbol{I}_{\mathrm{a}}$ and $\boldsymbol{V}_{\mathrm{ga}}$ are the vectors of the grid current and voltage in phase-a, respectively.

Fig. 11 shows the single-phase voltage vector diagram of the HCHB-ER according to (11), where the direction of the grid current vector $\boldsymbol{I}_{\mathrm{a}}$ is taken as the d-axis, and the direction of the grid filter inductance vector $\boldsymbol{V}_{\mathrm{Lf}}$ perpendicular to $\boldsymbol{I}_{\mathrm{a}}$ is taken as the q-axis to establish a d–q rectangular coordinate system. Then, the output voltage vector of the proposed HCHB-ER can be decomposed into two mutually perpendicular vectors based on the direction of grid current.

Among them, the active voltage vectors of the PV and ES module in the d-axis in the same direction as $\boldsymbol{I}_{\mathrm{a}}$ are identified as $\boldsymbol{u}_{\mathrm{pv\_smaid}}$ and $\boldsymbol{u}_{\mathrm{es\_smaid}}$, respectively, and the reactive voltage vectors of the PV and ES module in the q-axis perpendicular to $\boldsymbol{I}_{\mathrm{a}}$ are identified as $\boldsymbol{u}_{\mathrm{pv\_smaiq}}$ and $\boldsymbol{u}_{\mathrm{es\_smaiq}}$, respectively.

Therefore, (11) can be further decomposed into

$$\begin{cases} \boldsymbol{V}_{\mathrm{Na}} = V_{\mathrm{Nad}} + jV_{\mathrm{Naq}} \\ V_{\mathrm{Nad}} = \sum_{i=1}^{n} S_{\mathrm{pv\_aid}} U_{\mathrm{pv\_csmai}} + \sum_{j=1}^{m} S_{\mathrm{es\_ajd}} U_{\mathrm{es\_csmaj}} \\ V_{\mathrm{Naq}} = \sum_{i=1}^{n} S_{\mathrm{pv\_aiq}} U_{\mathrm{pv\_csmai}} + \sum_{j=1}^{m} S_{\mathrm{es\_ajq}} U_{\mathrm{es\_csmaj}}. \end{cases} \tag{12}$$

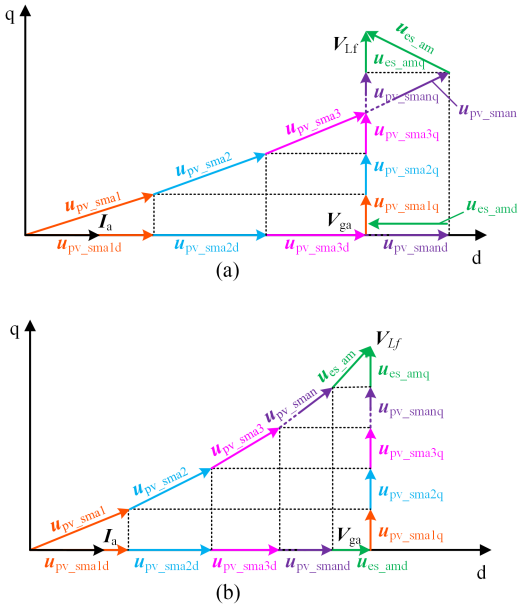

Fig. 11. Single-phase voltage vector diagram of HCHB-ER. (a) ES-SMs supplying power. (b) ES-SMs absorbing power.

For single-phase CHB, it is essential to maintain the dc-side voltage balance to ensure stable system operation in the intraphase. Various methods have been proposed in the literature [16] to address the intermodule power imbalance. In the proposed topology, the active voltage vectors of the PV and ES modules are proportional to their input power, and the reactive voltage vectors are equally distributed in each module to handle the intraphase power imbalance over a wide range.

Taking the kth PV-SM (or ES-SM) in phase-a as an example, the active and reactive power transmitted by it to ac-side are $P_{\mathrm{pv/es\_ak}}$ and $Q_{\mathrm{pv/es\_ak}}$, and the total active and reactive power of the converter are P_{a} and Q_{a}. Then, the kth PV (or ES) module modulation ratio vector can be expressed as

$$\begin{cases} \boldsymbol{S}_{\mathrm{pv/es\_ak}} = S_{\mathrm{pv/es\_akd}} + jS_{\mathrm{pv/es\_akq}} \\ S_{\mathrm{pv/es\_akd}} = \dfrac{(n+m)P_{\mathrm{pv/es\_ak}}}{P_a} g\cos\varphi \\ S_{\mathrm{pv/es\_akq}} = g\sin\varphi \end{cases} \tag{13}$$

where g is the converter output voltage modulation ratio. As can be seen from Fig. 11(a) where the PV output active power is greater than the average value of each phase, the ES-SMs modulate the opposite active voltage vector to absorb the additional active power. Similarly, when the PV output power is insufficient, the ES-SM modulates the active voltage vector in phase with the PV-SMs to replenish the power.

The KVL equation of the traditional three-phase CHB-PV has been established in Section II. The three-phase node voltage equation of the HCHB-ER can be written by referring to this method, which will not be discussed in detail. In the following, the grid-connected power is assumed to be constant, and the three-phase voltage vector diagram of the proposed topology operating under general operating condition are given to illustrate the energy control strategy.

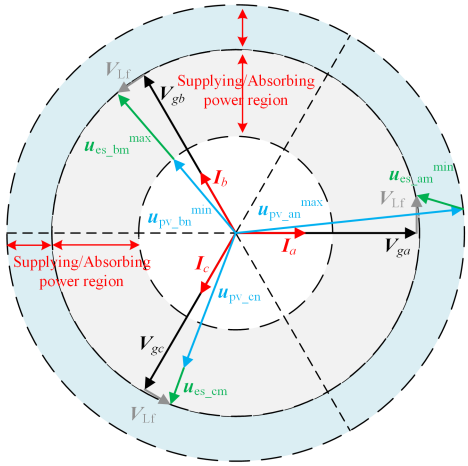

Fig. 12. Three-phase voltage vector diagram of the proposed HCHB-ER.

As shown in Fig. 12 where the PV output power of phase-a increases to the maximum power and phase-b decreases to the minimum power, the ES-SMs of phases a and b are activated. The ES-SMs provide maximum (minimum) power is related to both the CES SOC and the power limitation of ES-SMs. Therefore, taking the maximum and minimum power of ES-SMs as the radius, the ES-SMs supplying and absorbing power region of the three-phase can be drawn, as shown in the gray and blue parts of Fig. 12, where $\boldsymbol{u}_{\mathrm{es\_xm}}{}^{\mathrm{max}}$ and $\boldsymbol{u}_{\mathrm{es\_xm}}{}^{\mathrm{min}}$ represent the maximum and minimum output voltage of ES-SMs, and $\boldsymbol{u}_{\mathrm{pv\_xm}}{}^{\mathrm{min}}$ and $\boldsymbol{u}_{\mathrm{pv\_xm}}{}^{\mathrm{max}}$ represent the minimum and maximum output voltage of the PV-SMs. Similarly, the PV output power of phase-c decreases, and the ES-SMs of phase-c need to supply power, which satisfies the power balance region and ensures the stable operation of the system.

The filter inductance has little impact on the converter output voltage, so in order to simplify the analysis of the power transfer characteristic, it is assumed that the converter output voltage is in the same phase as the grid voltage. Therefore, the converter output power of phase-a is

$$\begin{aligned} P_{\mathrm{a}} &= P_{\mathrm{pv\_a}} + P_{\mathrm{es\_a}} \\ &\Leftrightarrow \frac{1}{2}U_{\mathrm{Na}}I_a = \frac{1}{2}(U_{\mathrm{pv\_an}} + U_{\mathrm{es\_am}})I_a \\ &= U_{\mathrm{csm}}\left(\sum_{i=1}^{n} i_{\mathrm{pv\_sma}i} + \sum_{j=1}^{m} i_{\mathrm{es\_sma}j}\right) \\ &= \sum_{i=1}^{n} U_{\mathrm{pva}i}I_{\mathrm{pva}i} + \sum_{i=1}^{n} U_{\mathrm{es}}I_{\mathrm{esa}j} \end{aligned} \tag{14}$$

where P_{a}, $P_{\mathrm{pv\_a}}$, and $P_{\mathrm{es\_a}}$ are output power of all SM, PV-SMs, and ES-SMs of phase-a, respectively, I_{a} is the grid current amplitude, U_{Na} is the converter output voltage amplitude, $U_{\mathrm{pv\_an}}$ and $U_{\mathrm{es\_am}}$ are the output voltage amplitudes of all PV-SMs and ES-SMs, respectively, and U_{csm} is the average capacitance voltage of the SM.

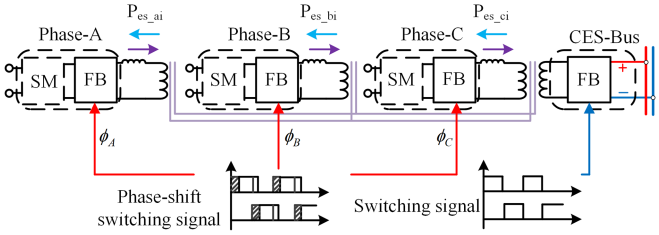

Fig. 13. Power transmission equivalent mode of QAB.

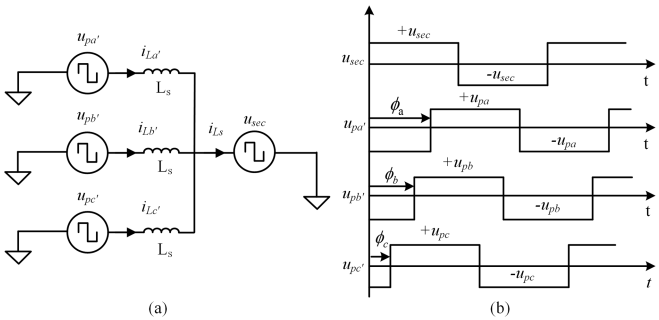

Fig. 14. Power transfer model of QAB. (a) Equivalent model. (b) Modulation strategy.

The single-phase output power (14) has been discussed above. In the proposed topology, the CES transmits power to the three-phase horizontal ES-SMs through QAB. The equivalent model and modulation strategy of QAB power transfer model are established in Fig. 13, in which phase shift modulation with 50% duty cycle is adopted for the power transmission between secondary CES and primary three SMs. The QAB equivalent model is shown in Fig. 14(a), and the QAB modulation strategy is shown in Fig. 14(b).

It can be seen that the phase shift angle φ determines the magnitude and direction of the power transfer between the primary SM and the secondary CES. The jth ES-SM power in phase-a $P_{\mathrm{es\_xj}}$ transferred from the primary port ($u = a', b', c'$) to the secondary port ($v = \mathrm{sec}$) has been derived in [32], which can be expressed as follows:

$$P_{\mathrm{es\_xj}} = \frac{n_{\mathrm{ps}} U_{\mathrm{csm}} U_{\mathrm{es}}}{2 f_{\mathrm{s}} L_{\mathrm{s}}} \frac{\phi_{\mathrm{x}}}{\pi} \left(1 - \frac{|\phi_{\mathrm{x}}|}{\pi}\right) \tag{15}$$

where n_{ps} is the turn ratio of primary and secondary winding of high-frequency transformer of QAB, f_{s} is the high-frequency transformer switching frequency of QAB, φ_{x} is the phase shift angle of QAB, and L_{s} is the phase shift inductance of QAB.

The interphase power balance of CHB converter can be realized, by adjusting the power of the configured ES-SMs. The ES-SMs reference power of each phase can be obtained as

$$P_x = \sum_{i=1}^{n} U_{\mathrm{pv\_xi}} I_{\mathrm{pv\_xi}} + \sum_{i=1}^{n} U_{\mathrm{es}} I^*_{\mathrm{es\_xj}} = \sum_{i=1}^{n} P_{\mathrm{pv\_xi}} + \sum_{i=1}^{n} P^*_{\mathrm{es\_xj}}$$

$$\Leftrightarrow P^*_{\mathrm{es\_x}} = \frac{P_{\mathrm{ac}}}{3} - P_{\mathrm{pv\_x}} \tag{16}$$

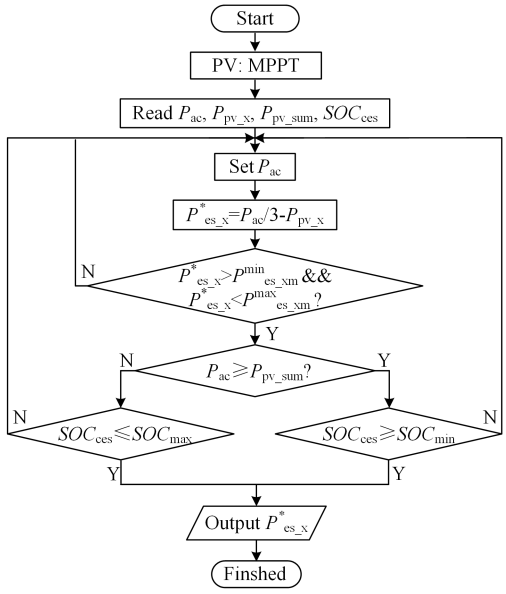

Fig. 15. Flowchart of the CES power management algorithm.

where $P_{\mathrm{x}} = P_{\mathrm{a}} = P_{\mathrm{b}} = P_{\mathrm{c}} = P_{\mathrm{ac}}/3$; P_{ac} is the grid power of the CHB converter, the selection that is related to the proposed HCHB-ER operation mode. There are two operating modes in the proposed topology: 1) follow-up and 2) power scheduling. In the follow-up model, the converter output power is the PV output power in real time. In this model, the CES is only acting as an intermediary power regulator without affecting the overall SOC, and the grid power P_{ac} is

$$P_{\mathrm{ac}} = \frac{l_{\mathrm{a}} + l_{\mathrm{b}} + l_{\mathrm{c}}}{3} \times \frac{P_{\mathrm{N}}}{3}. \tag{17}$$

In the power scheduling model, the ES-SMs reference power is not only related to the degree of interphase power imbalance but also closely related to the upper grid side scheduling, which will have an impact on the SOC of CES. Therefore, there are also two important constraints that should be considered in the proposed HCHB-ER. The SOC constraint of the CES determines whether the ES can operate over a long time, and the power limit constraint of the ES-SMs determines whether the proposed system can operate stably.

The flowchart of the CES power management algorithm is shown in Fig. 15. It can be seen that the upper power scheduling and interphase power balancing are achieved by controlling the ES-SMs power. However, when the SOC of CES exceeds its maximum (or maximum) range, the grid power should be reset based on the PV output power to discharge (or charge) the CES so that the SOC level remains desirable. Simultaneously, it is imperative to ensure that the power reference of ES-SMs in every phase complies with the intrapower regulation boundary, which will be analyzed in detail in the subsequent section.

C. Intrapower Regulation for Imbalance Constraints

In the above analysis, the configured ES-SMs eliminate the interphase power imbalanced of the CHB-PV, which requires

bidirectional power transfer between the CES and the configured ES-SMs. Under carrier phase shift sinusoidal pulsewidth modulation (PWM), when power is transferred between different SMs in the same phase with opposite polarity, the system operation must satisfy three types of constraints: SMs voltage constraint, converter output voltage constraint, and PV and ES SMs power balance constraint. Failure to meet these requirements will result in unstable system operation.

According to the proposed HCHB-ER topology shown in Fig. 9, there are $n + m$ SMs in one phase of the HCHB-ER and $K = m/n$ is used to denote the ratio of the number of ES-SMs and PV-SMs.

1) *SMs Voltage Constraint*: For the first constraint, it is assumed that the SM capacitor is large enough to suppress the SM voltage double frequency ripple. The SM output voltage is bipolar and the SM output voltage constraint of PV-SMs and ES-SMs can be expressed as the following, respectively:

$$\begin{cases} |u_{\text{pv\_xn}}(t)| \le n \times U_{\text{csm}} \\ |u_{\text{es\_xm}}(t)| \le m \times U_{\text{csm}}. \end{cases} \tag{18}$$

2) *Converter Output Voltage Constraint:* Since the instantaneous output voltage of all PV and ES SMs in one phase together constitutes the instantaneous converter output voltage, under the constraints of SMs output voltage, the converter output voltage constraint should also be satisfied

$$u_{\text{Nx}}(t) = u_{\text{pv\_xn}}(t) + u_{\text{es\_xm}}(t). \tag{19}$$

3) *SMs Power Balance Constraint*: The last constraint is the most important in three kinds of constraints. In the following, the power balance constraints between PV and ES SMs are analyzed from the perspective of topology configuration. It is assumed that the conventional CHB-PV converter has n SMs, which are connected to n distributed PV areas, and the sum capacitor voltage of all SMs in one phase is $U_{\text{dc}} = nU_{\text{csm}}$. The number of m ES-SMs is added to the original n PV-SMs, and the sum of the capacitor voltage of all SMs in one phase is changed to $U_{\text{sum\_dc}} = (n + m)U_{\text{csm}} = (1 + K)U_{\text{dc}}$.

When the power of PV panel and CES power is injected into the SM through dc–dc converter, the average charging power of the SM capacitor should be zero in line frequency period, otherwise it will cause the SM capacitor voltage to deviate from the reference voltage, resulting in unstable system operation. Therefore, the input power of SMs from dc/dc converter and output power to ac side should be balanced, and the constraint can be obtained as

$$P_{\text{pv\_xn}}^{\text{inj}} = \underbrace{\frac{1}{T_s}\int_{-\frac{T_s}{2}}^{\frac{T_s}{2}} u_{\text{pv\_xn}}(t) i_x(t) dt}_{P_{\text{pv\_xn}}} \tag{20}$$

$$P_{\text{es\_xm}}^{\text{inj}} = \underbrace{\frac{1}{T_s}\int_{-\frac{T_s}{2}}^{\frac{T_s}{2}} u_{\text{es\_xm}}(t) i_x(t) dt}_{P_{\text{es\_xm}}} \tag{21}$$

where T_s represents the line frequency period of the grid current, $P_{\text{pv\_xn}}$ and $P_{\text{es\_xm}}$ (x represents a, b, and c) are the average active output power of PV-SMs and ES-SMs, respectively, and ${P_{\text{pv\_xn}}}^{\text{inj}}$ and ${P_{\text{es\_xm}}}^{\text{inj}}$ are the PV panel and CES average power injected into the PV-SMs and ES-SMs.

D. Intrapower Regulation for Imbalance Boundary

In order to satisfy (20) and (21), it is necessary to ensure that the maximum output power ${P_{\text{pv\_xn}}}^{\text{max}}$ of n PV-SMs is greater than the PV panel injected power and the minimum (or maximum) output power ${P_{\text{es\_xm}}}^{\text{min}}$ (or ${P_{\text{es\_xm}}}^{\text{max}}$) of m ES-SMs is greater than the CES charging power (or discharging). It should be noted that when the configured ES-SMs output power, it is equivalent to the role of the PV-SMs, which is the same constraint as the PV-SMs. Thus, the power constraint is

$$P_{\text{pv\_xn}}^{\text{max}} \ge P_{\text{pv\_xn}}^{\text{inj}} \tag{22}$$

$$\left|P_{\text{es\_xm}}^{\text{min}}\right| \ge \left|P_{\text{es\_xm}}^{\text{inj}}\right|. \tag{23}$$

According to (22) and (23), it is necessary to solve the maximum and minimum output power of PV-SMs and ES-SMs in one phase. When the configured ES-SMs are used for power supplement, it is the same constraint condition as the PV-SMs. Therefore, this section takes phase-a as an example to discuss the maximum and minimum power of the ES-SMs in detail. To simplify the analysis, the influence of power factor angle φ and filter inductance L_{f} is ignored, that is, the reactive power of the converter $Q = 0$, and the output voltage and grid-connected current of the converter are expressed as follows:

$$\begin{cases} u_{\text{Na}}(t) = U_{\text{Na}} \cos(\omega t) = gU_{\text{sum\_dc}} \cos(\omega t) \\ i_{\text{a}}(t) = I_{\text{a}} \cos(\omega t) \end{cases} \tag{24}$$

where g is the converter output voltage modulation ratio and U_{Na} is the converter output voltage amplitude. After a certain number of ES-SMs are configured in CHB converter, the power limit analysis can be divided into two modes according to the modulation ratio range of the HCHB-ER: Mode 1 ($g >= 1/(1 + K)$), the converter works in high modulation ratio mode, which requires the configured ES-SMs and PV-SMs to participate together to achieve the converter output voltage, i.e., $U_{\text{Na}} >= U_{\text{dc}}$; Mode 2 ($g < 1/(1 + K)$), the converter works in low modulation ratio mode, n PV-SMs can satisfy the modulation and ES-SM do not need to participate in the modulation, i.e., $U_{\text{Na}} < U_{\text{dc}}$.

Fig. 16 shows the output voltage and current waveforms of the converter in Mode 1, where the color of gray represents the output voltage capabilities of ES-SMs, and the color of purple represents the output voltage capability of PV-SMs.

In this section, the ES-SMs minimum power in Mode 1 is taken as an example to analyze its power limit in detail. Due to the symmetry of the grid current and converter output voltage, the analysis only needs to be done in [$-\pi$, $-\pi/2$]:

Interval I [$-\pi$, ωt_2): Grid current is negative and the output voltage of ES-SMs is expected to be positive when analyzing the ${P_{\text{es\_am}}}^{\text{min}}$, i.e., the ES-SMs absorb energy from the grid side. However, due to the converter output voltage constraints, the ES-SMs must output negative voltage to meet the converter output voltage requirement, i.e., ${u_{\text{es\_am}}}^{\text{min}}(t) = u_{\text{Na}}(t) + U_{\text{dc}}$.

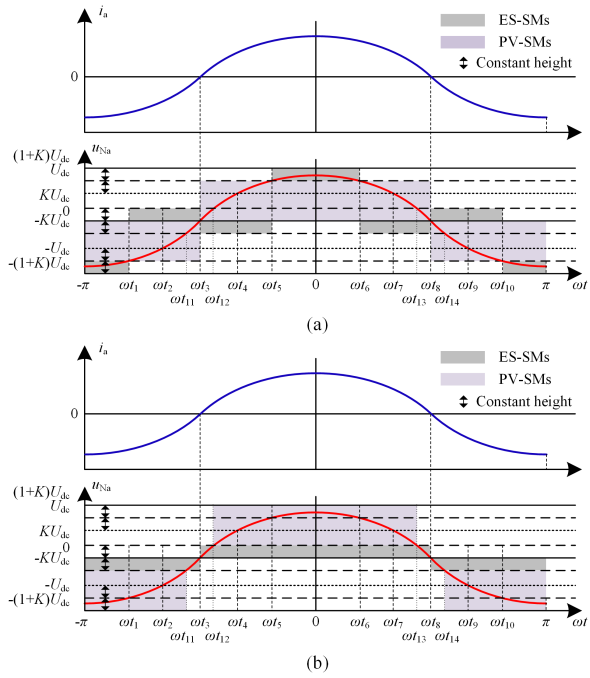

Fig. 16. Output voltage and current waveforms in Mode 1. (a) ES-SMs minimum power. (b) ES-SMs maximum power.

Interval II $[\omega t_2, \omega t_3)$: Grid current is negative and the output voltage of ES-SMs is expected to be positive when analyzing the $P_{\text{es\_am}}{}^{\min}$. However, due to the SMs voltage constraints, the ES-SMs output voltage is $u_{\text{es\_am}}{}^{\min}(t) = KU_{\text{dc}}$.

After the analysis of the specific operating conditions, the general theory of minimum and maximum power of ES-SMs is derived. Since the SM output voltage is bipolar, when grid current is positive ($i_{\text{x}} \geq 0$) and analyzes the $P_{\text{es\_xm}}{}^{\min}$, the ES-SMs output voltage $u_{\text{es\_xm}}$ is expected to output the maximum voltage $-KU_{\text{dc}}$. However, under the constraint of SMs output voltage and converter output voltage, $u_{\text{es\_xm}}$ cannot output the maximum voltage that even needs to output a certain positive voltage to meet the converter output voltage constraint. The principle for $i_{\text{x}} < 0$ is the same as $i_{\text{x}} \geq 0$

$$P_{\text{es\_xm}}^{\min} = \frac{1}{T_s}\int_{-\frac{T_s}{2}}^{\frac{T_s}{2}} u_{\text{es\_xm}}^{\min}(t) i_x(t) dt \tag{25}$$

$$u_{\text{es\_xm}}^{\min} = \begin{cases} \max[-KU_{\text{dc}}, u_{\text{Nx}} - U_{\text{dc}}] & \text{for} \quad i_x \geq 0 \\ \min[KU_{\text{dc}}, u_{\text{Nx}} + U_{\text{dc}}] & \text{for} \quad i_x < 0. \end{cases} \tag{26}$$

Similarly, the expression of $P_{\text{es\_xm}}{}^{\max}$ can be derived as follows:

$$P_{\text{es\_xm}}^{\max} = \frac{1}{T_{\text{s}}}\int_{-\frac{T_s}{2}}^{\frac{T_s}{2}} u_{\text{es\_xm}}^{\max}(t) i_{\text{x}}(t) dt \tag{27}$$

$$u_{\text{es\_xm}}^{\max} = \begin{cases} \min[KU_{\text{dc}}, u_{\text{Nx}} + U_{\text{dc}}] & \text{for} \quad i_{\text{x}} \geq 0 \\ \max[-KU_{\text{dc}}, u_{\text{Nx}} - U_{\text{dc}}] & \text{for} \quad i_{\text{x}} < 0 \end{cases} \tag{28}$$

where $u_{\text{es\_am}}{}^{\max}$ is the maximum voltage of ES-SMs.

IV. Assessment of Power Imbalance Regulation Capability

A. State-of-the-Art Injection Methods

To determine the zero-sequence injection method with optimal power balance capability, the PBF and PBS are utilized to assess the converter power balance performance under various zero-sequence injection methods as referenced in [24].

In Section II-B, l_{x} has been defined as the PV generation coefficient of each phase, with a value range between 0 to 1. Therefore, taking the three-phase PV generation power coefficient l_{a}, l_{b}, l_{c} as the x, y, and z axes, the 3-D coordinates of $1 \times 1 \times 1$ can be established. When l_{a}, l_{b}, and l_{c} are not equal, the zero-sequence voltage is injected into the converter output voltage, whose amplitude and phase are related to the degree of interphase power imbalance. However, due to the dc-side constraint, the converter output voltage should be less than the sum of the sum of the available dc-side voltage

$$\max\{v_{\text{Na}}, v_{\text{Nb}}, v_{\text{Nc}}\}(l_{\text{a}}, l_{\text{b}}, l_{\text{c}}) \leq nU_{\text{csm}}. \tag{29}$$

All points that can be rebalanced by the injected zero-sequence voltage components can form a 3-D space defined as PBS, and the volume is called PBF

$$\text{PBF} = \int_0^1 \int_0^1 \int_0^1 F(l_{\text{a}}, l_{\text{b}}, l_{\text{c}}) dl_{\text{a}} dl_{\text{b}} dl_{\text{c}} \tag{30}$$

$$F(l_{\text{a}}, l_{\text{b}}, l_{\text{c}}) = \begin{cases} 1, & \max\{v_{\text{Na}}, v_{\text{Nb}}, v_{\text{Nc}}\}(l_{\text{a}}, l_{\text{b}}, l_{\text{c}}) \leq nU_{\text{csm}} \\ 0, & \max\{v_{\text{Na}}, v_{\text{Nb}}, v_{\text{Nc}}\}(l_{\text{a}}, l_{\text{b}}, l_{\text{c}}) > nU_{\text{csm}}. \end{cases} \tag{31}$$

The larger the volume of PBS, the stronger the power balancing capability. In order to better compare the power balance capability of different zero-sequence injection methods under different working conditions, the work in [21] defines two more generalized normalized parameters: the filter inductance $L_{\text{f(p.u.)}}$ and the voltage overrating ε

$$L_{\text{f(p.u.)}} = \frac{2\pi f L_{\text{f}} P_{\text{N}}}{3V_{\text{g}}} \tag{32}$$

$$\varepsilon = \frac{nU_{\text{csm}}}{\sqrt{2}V_{\text{g}}\sqrt{1 + L_{\text{f(p.u.)}}^2}} - 1 \tag{33}$$

where (29) can be rewritten as follows:

$$\max\{v_{\text{Na}}, v_{\text{Nb}}, v_{\text{Nc}}\}(l_{\text{a}}, l_{\text{b}}, l_{\text{c}}) \leq \sqrt{2}V_{\text{g}}(\varepsilon + 1)\sqrt{1 + L_{\text{f(p.u.)}}^2}. \tag{34}$$

The PBS and PBF of different injection methods in the case of $\varepsilon = 10\%$ are shown in [21]. It can be seen from the figure that the PBF of FFZSI is the weakest of 4%. RTHI and DTHI improve the power balance capability of FFZSI to 15% after the THI. OZSI has the best power balance capability, of which PBF is 20%. Fig. 17 shows the PBF line chart of different zero-sequence injection methods under the same ε and different filter inductance $L_{\text{f(p.u.)}}$ values, which indicate that the filter inductance $L_{\text{f(p.u.)}}$ has little influence on the PBF and can be neglected.

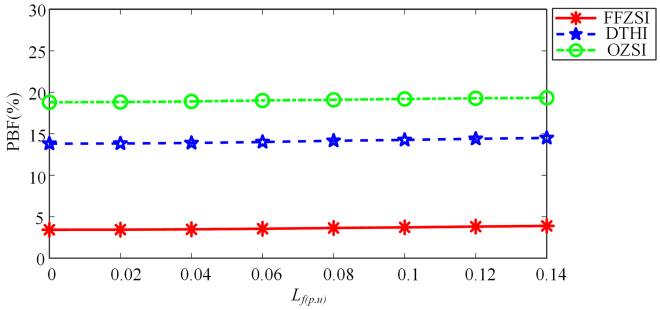

Fig. 17. PBF of different injection methods under the same $\varepsilon = 10\%$ and different filter inductance $L_{\mathrm{f(p.u.)}}$.

Among all the zero-sequence voltage injection strategies, FFZSI is the most fundamental and straightforward method to implement. However, its PBF is relatively weak compared to other injection methods. On the other hand, OZSI exhibits superior power balance capability among all injection techniques but requires repeated calculation iterations when seeking optimal phase angle, which poses a challenge for computing resources and real time computing ability of the controller.

B. Proposed Hybrid CHB-ER

The proposed HCHB-ER, which integrates PV and ES into a single converter, effectively eliminates interphase power imbalances and facilitates upper-layer power scheduling. In this section, the PBS of the proposed HCHB-ER topology is compared with the existing injection method, and in the actual engineering application, how to decide the ratio of PV and ES modules to achieve the maximum power balance capability is analyzed in the following.

The main power balance capability constraint of the zero-sequence voltage injection methods is the dc-side voltage. However, the proposed HCHB-ER topology power balance capability constraint is the maximum power absorbed or released by ES-SMs, and the constraint expression can be derived as

$$P_{\mathrm{es\_xm}}^{\mathrm{max}} \geq P_{\mathrm{es\_xm}}^{\mathrm{inj}} \tag{35}$$

$$P_{\mathrm{es\_xm}}^{\mathrm{min}} \leq P_{\mathrm{es\_xm}}^{\mathrm{inj}}. \tag{36}$$

When analyzing the PBF and configuration ratio of the topology proposed in this article, in order to make the conclusion more general, a new definition $K = m/n$, which is the ratio of the configured ES-SM and the PV-SM is added to ε. Based on the above analysis of the maximum intrapower regulation boundary, Fig. 18 shows the relationship diagram of ε, K, and ${P_{\mathrm{es\_xm}}}^{\mathrm{min}}$ where the minimum power of the ES-SMs is standardized based on the rated of each phase ($P_{\mathrm{ac}}/3$). Fig. 18(b) shows that when K is fixed, the minimum value of ${P_{\mathrm{es\_xm}}}^{\mathrm{min}}$ first decreases and then increases with the increase of ε. As shown in Fig. 18(c), when ε is fixed, the maximum power of the ES modules ${P_{\mathrm{es\_xm}}}^{\mathrm{min}}$ increases with the K, but when the ratio of ES and PV modules $K =$ 0.4, the power of the ES-SMs reaches the minimum value about 0.68, and then the power of the ES-SMs decreases continuously with the increase of K.

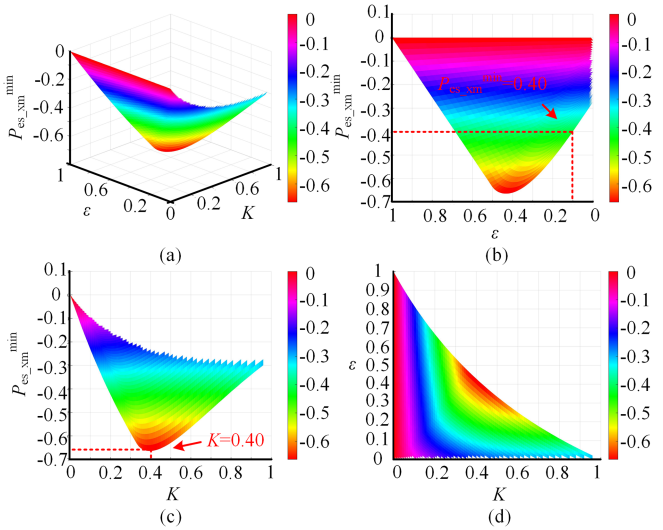

Fig. 18. Relationship diagram of ε, K, and ${P_{\mathrm{es\_xm}}}^{\mathrm{min}}$. (a) 3-D view. (b) y–z view. (c) x–z view. (d) x–y view.

To sum up, under different ε, the power regulation range of the ES can be expanded by a reasonable selection of the ratio K value. However, when the number of ES-SMs is too large, even exceeding the PV-SMs ($K > 1$), some ES-SMs can no longer provide power bidirectional regulation and can only be used for power supplement due to power limit constraints. Therefore, the interphase power balance capability can effectively improve by configuring a small number of ES-SMs and keeping the value of K within a reasonable range.

The PBS of the proposed topology is analyzed with PV operating at $\varepsilon = 10\%$, where the ratio K of ES and PV modules is determined by the configuration constraints analyzed in Fig. 18. Therefore, when the PV-SMs operate under the condition of ε = 10% and the configuration factor $K = 0.75$ of the ES and PV module, the ES-SMs interphase power regulation capability reaches the maximum. Fig. 19 plots PBS and PBF of the proposed topology under three different configurations of $K = 0.25$, 0.5, and 0.75. It can be seen from the figure that when $K = 0.25$, the PBF is 20.14%, which is approximately equal to the PBF of the OZSI. When $K = 0.75$, the maximum PBF is 45.85%, whereas the maximum PBF is only 20% in all zero-sequence voltage injection strategies. Compared with the zero-sequence voltage injection strategies, the proposed HCHB-ER topology significantly improves the PBS and PBF.

C. Comparison With Other ES Topology Schemes

In recent years, besides the zero-sequence voltage injection methods, configuring ES modules in each PV SM can also eliminate the imbalance power [29], [30], [31]. The decentralized battery topology scheme can be divided into two types: a single-stage type [29], as depicted in Fig. 20(a), and a two-stage type [30], as shown in Fig. 20(b).

In order to further verify the effectiveness of the proposed topology and centralized battery system, this article takes the

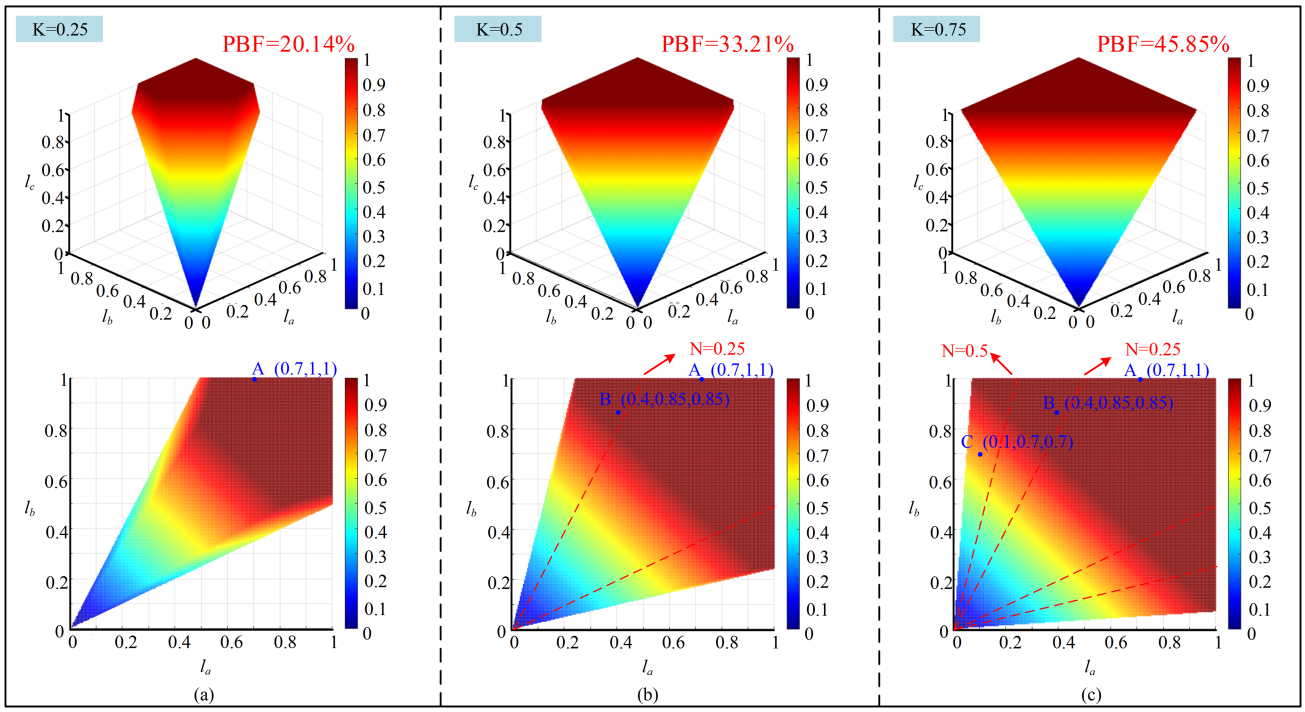

Fig. 19. PBS and PBF of the HCHB-ER with different configuration K under $\varepsilon = 10\%$. (a) $K = 0.25$. (b) $K = 0.5$. (c) $K = 0.75$.

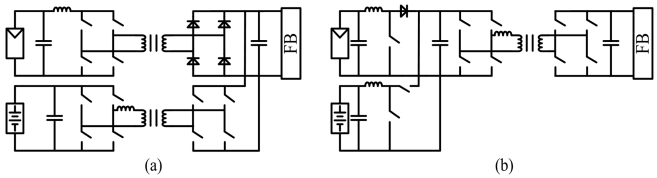

Fig. 20. Existing two types decentralized of CHB-PV/ES. (a) Single-stage type [29]. (b) Two-stage type [30].

TABLE II
DESIGN AND COMPARISON RESULTS OF THREE TYPES CHB-PV/ES SYSTEM

Project	CHB-PV/ES system	Tubes+ Diodes	HFTs	ES type	SOC balancing
Zhangbei	Type I	Most	Most	Distributed	Needed
	Type II	Middle	Least	Distributed	Needed
	HCHB-ER	Least	Middle	Centralized	Not Needed

Zhangbei microgrid demonstration project based on PV/ES system listed in Section I-B as an example to compare the proposed topology and existing two systems in [29] and [30]. Zhangbei project has a PV power of 40 MW and ES power/capacity of 10 MW/10 MWh.

Table II presents the design and comparison result, which demonstrate that the proposed HCHB-ER exhibits remarkable flexibility and does not require strict consistency with the number of PV modules. Although the distributed battery system has similar power balancing capabilities with the proposed HCHB-ER, the component count of ES converter in HCHB-ER is significantly lower than the two types of distributed schemes. More importantly, the proposed topology has no battery SOC balancing challenge and no additional harmonic injection.

V. Simulation Results

In order to verify the effectiveness of the proposed HCHB-ER strategy and the correctness of the ES-SMs configuration constraints and its PBS analysis, the simulation platform under three different configurations K is established in PLECS, where the number of PV-SMs in each CHB converter phase remains consistent and the ES-SMs are arranged sequentially. The corresponding down-scaled experimental platform was also established, and parameters of both simulation and experiment are presented in Table III.

The following three cases depicted in the simulation below correspond to power coefficient points A–C, as indicated in Fig. 19, under different configurations of K. Each coordinate represents an unbalanced operating condition with progressively increasing degree of phase imbalance.

A. *Slight Interphase Power Imbalance* ($l_a = 0.7$, $l_b = 1$, $l_c = 1$, $K = 0.25$)

Fig. 21 shows the simulation waveforms of slight interphase power imbalance with $K = 0.25$. The simulation commences in a steady state, with all PV-SMs operating under identical rated conditions ($S = 1000$ W/m^2 and $T = 25$ °C). The output power of the CHB converter is evenly distributed, whereas the ES-SMs remain inactive. After $t = 0.6$ s, the power coefficient of the three-phase PV generation changing from rated condition to point A, the irradiance of all PV-SMs in phase-a decreases from 1000 to 700 W/m^2, which corresponding power is 70%

TABLE III
SIMULATION AND EXPERIMENT PARAMETER

Parameter	Simulation	Experiment
AC voltage/U_g	5.3 kV	140 V
SM capacitor voltage/U_{csm}	1.5 kV	40 V
PV-SM number/n	4	4
PV-SM peak power/P_{PV}	75 kW	200 W
PV-SMs rated peak power/P_{PV}	0.90 MW	2.4 kW
AC active power/P_{ac}	0.90 MW	2.4 kW
CES voltage/U_{ces}	750 V	24 V
Fundamental AC frequency/f_s	50 Hz	50 Hz
PWM carrier frequency/f_c	2k Hz	2 kHz
QAB switching frequency/f_q	10 kHz	10 kHz
Transformer turns ratio	8:8:8:4	2:2:2:1
Filter inductance/L	4 mH	1.2 mH
SM capacitance/C	2 mF	0.68 mF

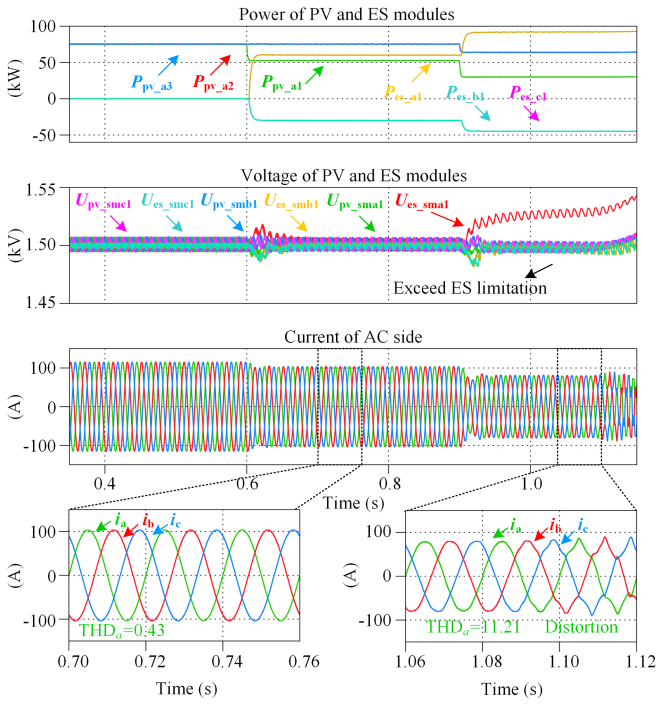

Fig. 21. Simulation waveforms of slight interphase power imbalance with $K = 0.25$.

of the peak power ignoring the effect of the loss caused by dc–dc converter, whereas the irradiance of all PV-SMs in phases b and c does not change. In the event of interphase power imbalance, the ES-SMs are activated. The CES receives 20% of phase-a power, whereas the ES-SMs in phases b and c absorb a portion of PV power to charge the CES. After a brief system adjustment, the grid current is restored to three-phase symmetry and the total harmonic distortion (THD) meets the requirements for grid current. At $t = 0.9$ s, the power coefficient transitions from point A to point B, surpassing the PBS at $K = 0.25$. Consequently, the CES desired power output cannot be achieved;

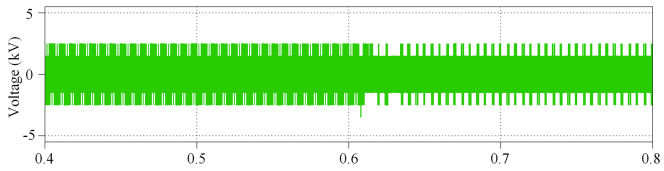

Fig. 22. Common-mode voltage waveforms of the proposed HCHB-ER under unbalanced conditions.

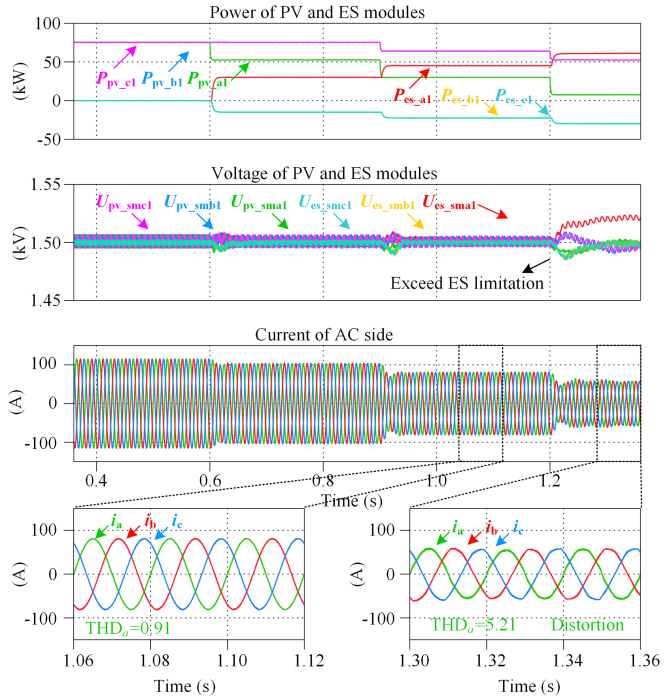

Fig. 23. Simulation waveforms of moderate interphase power imbalance with $K = 0.5$.

SMs capacitor voltage remains unbalanced; and grid-connected current distortion becomes severe.

Fig. 22 shows the common-mode voltage of the proposed HCHB-ER under unbalanced conditions. Compared with the common-mode voltage of the zero-sequence voltage injection methods, the proposed HCHB-ER does not change the common-mode voltage during interphase power imbalance, and three-phase current balance well, which is conducive to the smooth operation of the system.

B. Moderate Interphase Power Imbalance ($l_a = 0.4$, $l_b = 0.85$, $l_c = 0.85$, $K = 0.5$)

Fig. 23 shows the simulation waveforms of moderate interphase power imbalance with $K = 0.5$. Before $t = 0.9$ s, the power coefficient point of the three-phase PV generation is A, and the system operates stably. After $t = 0.9$ s, the power coefficient of the three-phase PV generation changes from point A to point B at which the irradiance of all PV-SMs in phase-a decrease from 700 to 400 W/m^2 and the irradiance of all PV-SMs in the other two phases decreases from 1000 to 850 W/m^2. The interphase imbalanced power is adjusted by the configured ES-SMs, which

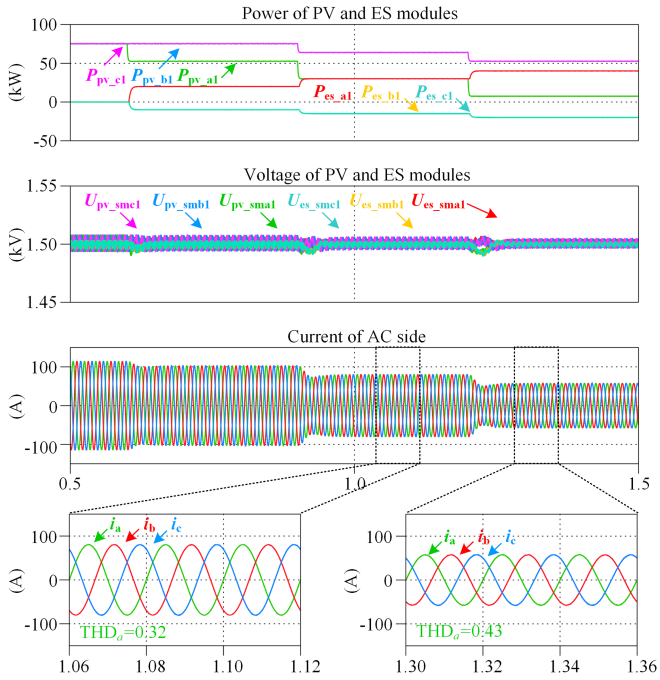

Fig. 24. Simulation waveforms of severe interphase power imbalance with $K = 0.75$.

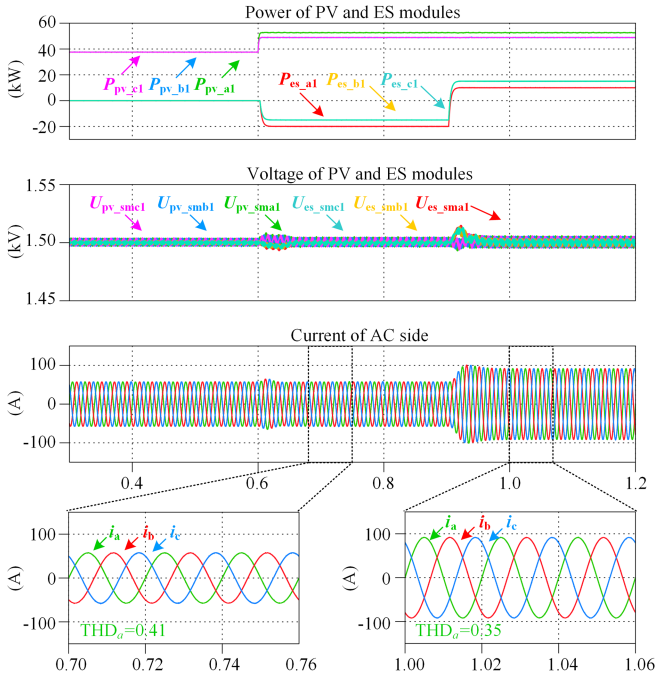

Fig. 25. Simulation waveforms of power scheduling response with $K = 0.75$.

provide 30% power in phase-a and absorb 15% power in the other two phases. After a brief system adjustment, the grid current is restored to three-phase symmetry and the THD meets the requirements for grid current. After $t = 1.2$ s, the PV power coefficient transitions from point B to point C, surpassing the PBS at $K = 0.5$. Consequently, the CES desired output power exceeds the limit constraint; the SMs capacitor voltage remains unbalanced; and grid-connected current distortion becomes severe.

C. Severe Interphase Power Imbalance ($l_a = 0.1$, $l_b = 0.7$, $l_c = 0.7$, $K = 0.75$)

Fig. 24 shows the simulation waveforms of severe interphase power imbalance with $K = 0.75$. At $t = 1.2$ s, the irradiance of all PV-SMs in phase-a decreases to 100 W/m^2 and the irradiance of all PV-SMs in the other two phases decreases from 850 to 700 W/m^2. The CES provides 30% power in phase-a and absorbs 30% power in phases b and c. As can be seen from Fig. 23, when $K = 0.75$, the system can well handle most imbalanced conditions, no matter under slight or severe interphase power imbalance. The results show that the voltage of SMs capacitors remains balanced, the grid-connected current waveform performs three-phase symmetry, and the THD meets the grid-connected requirements.

D. Power Scheduling Response

Fig. 25 shows the simulation waveforms of power scheduling response with $K = 0.75$. The simulation commences in a steady state, with all PV-SMs operating under the same condition ($S = 500$ W/m^2 and $T = 25$ °C), which is no power difference between

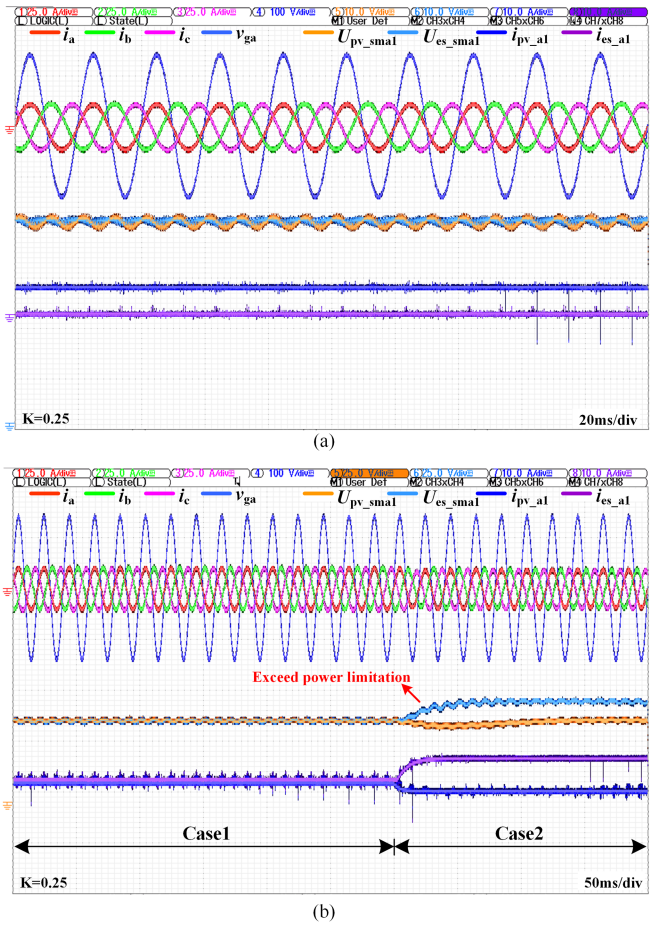

Fig. 26. Experimental waveforms with $K = 0.25$ in (a) balanced operation and (b) unbalanced operation.

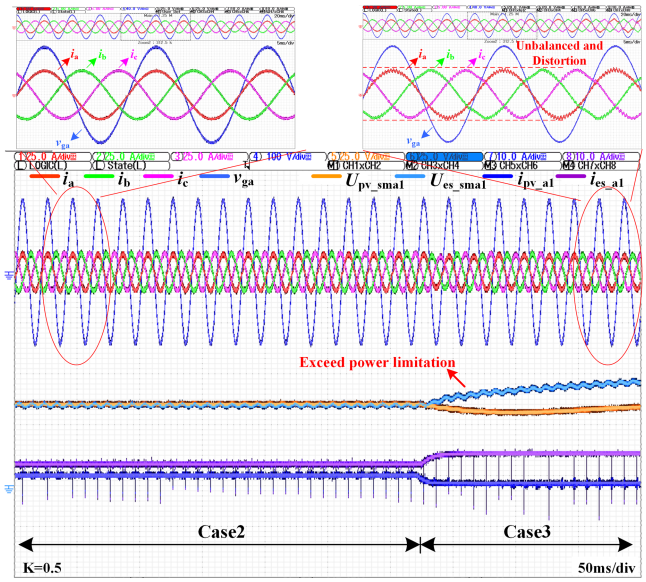

(a)

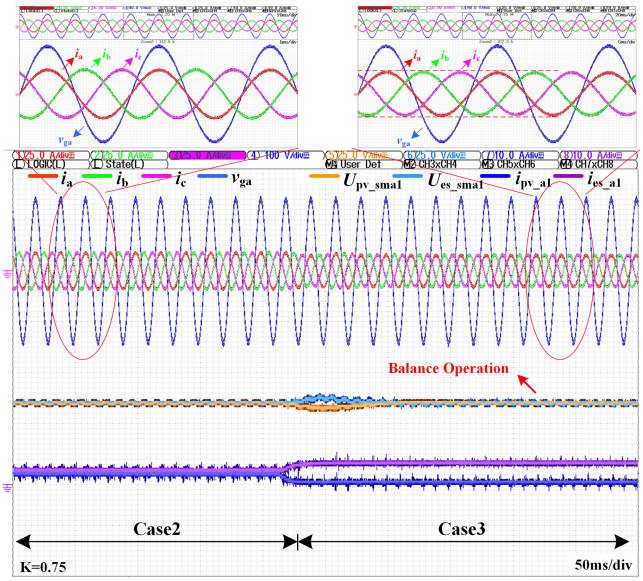

(b)

Fig. 27. Experimental waveforms with (a) $K = 0.5$ and (b) $K = 0.75$ in unbalanced operation.

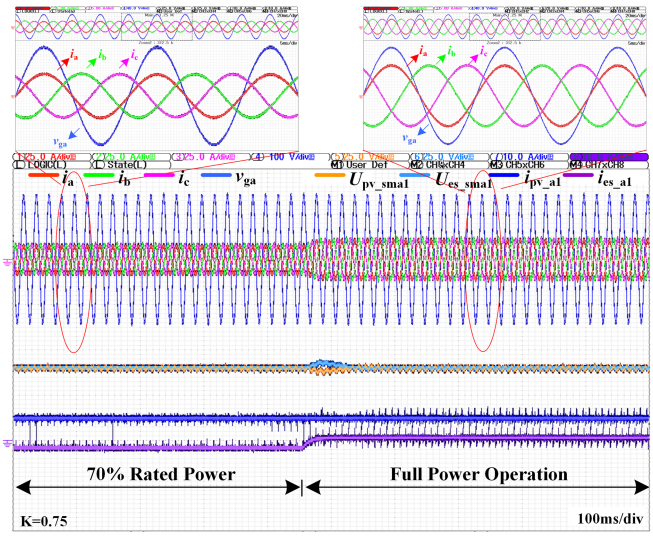

Fig. 28. Experimental waveforms of power scheduling response with $K = 0.75$.

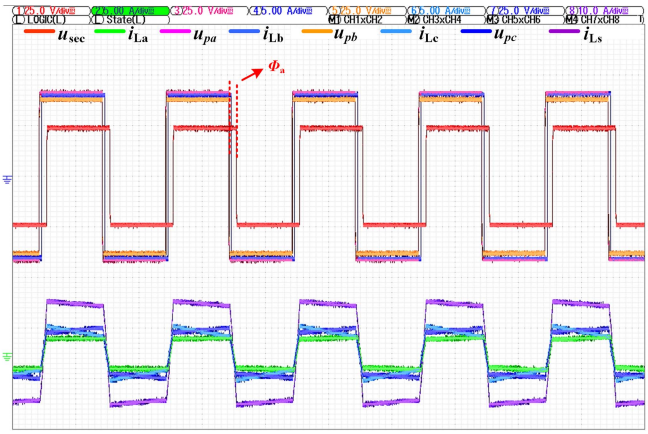

Fig. 29. Experimental waveforms of QAB.

phases. The grid-tied power demand is half of the rated PV peak power and the CES does not response. At $t = 0.6$ s, the grid-tied power demand not changing, the irradiance of all PV-SMs in phase-a rises from 500 to 700 W/m^2 and the irradiance of all PV-SMs in the other two phases also rises from 500 to 650 W/m^2. The CES not only assures the interphase power balance but also maintains the grid-tied power demand constant. The ES-SMs absorb 20% power in phase-a and 10% power in the other two phases. At $t = 0.9$ s, the grid-tied power demand changes to 80% rated PV peak power, and the PV output power not change. In response to the grid-tied scheduling requirement, the CES adjusts ES-SMs in phase-a to release 10% power, and ES-SMs in the other two phases to release 15% power. The results show that the voltage of the SMs capacitor remains balanced, the grid-connected current performs three-phase symmetry, and the grid-tied power meets the upper scheduling in real time.

VI. Experiment Results

Due to the limited laboratory conditions, this article sets up a power down-scaled experimental platform under different configurations for experimental verification, in which the number of PV-SMs in each phase is always 4, and the number of ES-SMs is increased in turn to verify the power balance capability of the system under different configurations. In the experiment, in order to simulate the PV power changes in different scenarios, each PV-SM in phase-a is connected to the programmable PV simulator, and the remaining PV-SMs in phases b and c are interconnected with 40 V switching power supply. During the experiment, the PV-SMs in phases b and c always output 200 W power. For the experimental platform control mechanism, TMS320F28377 is used as the master controller and

TMS320F28335 is used as the slave controller of the CHB converter, and the specific platform parameters are shown in Table III.

A. Balanced Power Generation

Fig. 26(a) shows the experimental waveforms with $K = 0.25$ in balanced operation in which all PV-SMs operate under the same nominal condition ($S = 1000$ W/m^2 and $T = 25$ °C) and the CES does not work. Each PV-SM injects 200 W power to the grid and the interphase output power is balanced. The grid-connected current tracks the grid voltage accurately, exhibiting three-phase symmetry in both amplitude and phase. Meanwhile, the SMs capacitor voltages are balanced and display double frequency ripple with the same amplitude.

B. Unbalanced Power Generation

The following is the comparison of the power balanced capability under different configurations K when the PV output power interphase is imbalanced:

Case 1: $l_a = 0.7$, $l_b = 1$, $l_c = 1$, $K = 0.25$.

Fig. 26(b) shows the experimental waveforms in Case 1, which is to verify the capability of the proposed HCHB-ER with $K = 0.25$ under slight interphase power imbalance, and the irradiance of all PV simulators in phase-a decreases from 1000 to 700 W/m^2. As shown in Fig. 26(b), when unbalanced condition occurs, the ES-SMs provide 20% power in phase-a to maintain the interphase power balanced and the grid current performs three-phase symmetry.

Case 2: $l_a = 0.4$, $l_b = 1$, $l_c = 1$, $K = 0.5$.

In order to verify the capability of the proposed HCHB-ER with $K = 0.5$ under moderate interphase power imbalance, the irradiance of all PV simulators in phase-a is continuously reduced from 700 to 400 W/m^2, and the output power of phases b and c is not changed. As shown in Fig. 26(b), when $K = 0.25$, the ES-SMs exceed the power limitation that leads capacitor voltage to deviate from the average and grid current distortion severely. However, when $K = 0.5$, the ES-SMs can provide better power adjustment range that avoids the power limitation. Therefore, as shown in Fig. 27(a), the grid current still performs symmetry and the capacitor voltage is well balanced.

Case 3: $l_a = 0.1$, $l_b = 1$, $l_c = 1$, $K = 0.75$.

In order to verify the capability of the proposed HCHB-ER with $K = 0.75$ under severe interphase power imbalance, the irradiance of all PV simulators in phase-a is continuously reduced from 400 to 100 W/m^2, and the output power of phases b and c is not changed. As shown in Fig. 27(a), when $K = 0.5$, the capacitor voltage deviates from the average, and the grid current distorts seriously. However, when $K = 0.75$, the ES-SMs can provide the best power adjustment range in three cases. As can be seen from Fig. 28(b), when severe interphase power imbalance occurs, the grid current still performs symmetry and capacitor voltage is balanced well.

C. Power Scheduling Response

Fig. 28 shows the experimental waveforms of power scheduling response with $K = 0.75$. At the initial stage, the irradiance of all PV simulators in phase-a is 900 W/m^2, and the irradiance of all PV simulators in phases b and c is 1000 W/m^2. The grid side power demand is 70% of rated power but the PV output power is greater than the power scheduling of the upper grid-side. Consequently, the ES-SMs in phase-a absorb 20% power and the ES-SM in the other two phases absorb 30% power. In the event that the upper power scheduling on the grid-side necessitates full system operation, it is incumbent upon the CES to supply sufficient power to meet demand. Fig. 28 shows that the proposed topology HCHB-ER can respond and track the upper power scheduling at the grid side in real time, maintain the interphase power balanced, and output the symmetrical three-phase grid-connected current.

Fig. 29 shows the modulation waveforms of QAB. When the upper grid-side requires system operating at power scheduling model, the CES transfers power to the three-phase horizontal ES-SMs of CHB through QAB. QAB adopts phase-shift modulation methods that can transfer different power to the ES-SMs in three-phase according to the imbalance degree of the interphase power and power scheduling from the upper grid side.

VII. Conclusion

This article presents a novel approach to CHB-based energy router hybrid PV and ES with a simple control strategy. The interphase power balance can be implemented by a small number of SMs interconnected with the CES. According to the imbalance state of the three-phase PV output power and grid-side power scheduling, the CES arbitrarily adjusts the ES-SMs to absorb or supply power to balance the interphase power and maintain the converter power stability. More importantly, under the three constraints from the modulation level, the intraphase power regulation boundary and the SM configuration ratios are analyzed in the hybrid configuration topology, which provides a security domain for the system stable operation.

The study of PBS of the proposed router with varying ratios of PV and ES modules shows that it can be significantly improved by integrating the ES inherent in the microgrids into the traditional CHB-PV, avoiding the appearance of overmodulation and common-mode voltage rise caused by traditional zero-sequence voltage injection methods. In addition, compared with the other modular distributed battery systems, the proposed hybrid configuration and CES system reduce the number of devices and avoid the SOC balancing challenge.

References

[1] W. Liang, Y. Liu, and J. Peng, "A day and night operational quasi-Z source multilevel grid-tied PV power system to achieve active and reactive power control," *IEEE Trans. Power Electron.*, vol. 36, no. 1, pp. 474–492, Jan. 2021.

[2] P. Pan et al., "An impedance-based stability assessment methodology for DC distribution power system with multivoltage levels," *IEEE Trans. Power Electron.*, vol. 35, no. 4, pp. 4033–4047, Apr. 2020.

[3] J. Yao, W. Chen, C. Xue, Y. Yuan, and T. Wang, "An ISOP hybrid DC transformer combining multiple SRCs and DAB converters to interconnect MVDC and LVDC distribution networks," *IEEE Trans. Power Electron.*, vol. 35, no. 11, pp. 11442–11452, Nov. 2020.
[4] M. S. Agamy et al., "A high power medium voltage resonant dual active bridge for MVDC ship power networks," *IEEE J. Emerg. Sel. Topics Power Electron.*, vol. 5, no. 1, pp. 88–99, Mar. 2017.
[5] J. I. Y. Ota, T. Sato, and H. Akagi, "Enhancement of performance, availability, and flexibility of a battery energy storage system based on a modular multilevel cascaded converter (MMCC-SSBC)," *IEEE Trans. Power Electron.*, vol. 31, no. 4, pp. 2791–2799, Apr. 2016.
[6] H. Akagi, "Classification, terminology, and application of the modular multilevel cascade converter (MMCC)," *IEEE Trans. Power Electron.*, vol. 26, no. 11, pp. 3119–3130, Nov. 2011.
[7] X. Zhang, M. Wang, T. Zhao, W. Mao, Y. Hu, and R. Cao, "Topological comparison and analysis of medium-voltage and high-power direct-linked PV inverter," *CES Trans. Elect. Mach. Syst.*, vol. 3, no. 4, pp. 327–334, Dec. 2019.
[8] K. Wang, R. Zhu, C. Wei, F. Liu, X. Wu, and M. Liserre, "Cascaded multilevel converter topology for large-scale photovoltaic system with balanced operation," *IEEE Trans. Ind. Electron.*, vol. 66, no. 10, pp. 7694–7705, Oct. 2019.
[9] A. C. Nair and B. G. Fernandes, "Solid-state transformer based fast charging station for various categories of electric vehicles with batteries of vastly different ratings," *IEEE Trans. Ind. Electron.*, vol. 68, no. 11, pp. 10400–10411, Nov. 2021.
[10] R. Sharma and A. Das, "Enhanced active power balancing capability of grid-connected solar PV fed cascaded H-bridge converter," *IEEE J. Emerg. Sel. Topics Power Electron.*, vol. 7, no. 4, pp. 2281–2291, Dec. 2019.
[11] M. Salehi, M. Shahabadini, H. Iman-Eini, and M. Liserre, "Predictive control of grid-connected modified-CHB with reserve batteries in photovoltaic application under asymmetric operating condition," *IEEE Trans. Ind. Electron.*, vol. 69, no. 9, pp. 9019–9028, Sep. 2022.
[12] H. D. Tafti, A. I. Maswood, G. Konstantinou, C. D. Townsend, P. Acuna, and J. Pou, "Flexible control of photovoltaic grid-connected cascaded H-bridge converters during unbalanced voltage sags," *IEEE Trans. Ind. Electron.*, vol. 65, no. 8, pp. 6229–6238, Aug. 2018.
[13] Z. Ye et al., "A novel DC-power control method for cascaded H-bridge multilevel inverter," *IEEE Trans. Ind. Electron.*, vol. 64, no. 9, pp. 6874–6884, Sep. 2017.
[14] C. Wang, K. Zhang, J. Xiong, Y. Xue, and W. Liu, "A coordinated compensation strategy for module mismatch of CHB-PV systems based on improved LS-PWM and reactive power injection," *IEEE Trans. Ind. Electron.*, vol. 66, no. 4, pp. 2825–2836, Apr. 2019.
[15] M. Wang et al., "Harmonic compensation strategy for single-phase cascaded H-bridge PV inverter under unbalanced power conditions," *IEEE Trans. Ind. Electron.*, vol. 67, no. 12, pp. 10474–10484, Dec. 2020.
[16] S. Yang et al., "Quantitative comparison and analysis of different power routing methods for single-phase cascaded H-bridge photovoltaic grid-connected inverter," *IEEE Trans. Power Electron.*, vol. 36, no. 4, pp. 4134–4152, Apr. 2021.
[17] T. J. Summers, R. E. Betz, and G. Mirzaeva, "Phase leg voltage balancing of a cascaded H-bridge converter based STATCOM using zero sequence injection," in *Proc. 13th Eur. Conf. Power Electron. Appl.*, Barcelona, Spain, 2009, pp. 1–10.
[18] Y. Yu et al., "On extending the energy balancing limit of multilevel cascaded H-bridge converters for large-scale photovoltaic farms," in *Proc. Australas. Univ. Power Eng. Conf.*, Hobart, TAS, Australia, 2013, pp. 1–6.
[19] Y. Yu, G. Konstantinou, B. Hredzak, and V. G. Agelidis, "Power balance of cascaded H-bridge multilevel converters for large-scale photovoltaic integration," *IEEE Trans. Power Electron.*, vol. 31, no. 1, pp. 292–303, Jan. 2016.
[20] Y. Yu, G. Konstantinou, B. Hredzak, and V. G. Agelidis, "Power balance optimization of cascaded H-bridge multilevel converters for large-scale photovoltaic integration," *IEEE Trans. Power Electron.*, vol. 31, no. 2, pp. 1108–1120, Feb. 2016.
[21] Y. Yu, G. Konstantinou, C. D. Townsend, and V. G. Agelidis, "Comparison of zero-sequence injection methods in cascaded H-bridge multilevel converters for large-scale photovoltaic integration," *IET Renewable Power Gener.*, vol. 11, no. 5, pp. 603–613, Apr. 2017.
[22] P. Sochor and H. Akagi, "Theoretical comparison in energy-balancing capability between star- and delta-configured modular multilevel cascade inverters for utility-scale photovoltaic systems," *IEEE Trans. Power Electron.*, vol. 31, no. 3, pp. 1980–1992, Mar. 2016.
[23] P. Sochor and H. Akagi, "Theoretical and experimental comparison between phase-shifted PWM and level-shifted PWM in a modular multilevel SDBC inverter for utility-scale photovoltaic applications," *IEEE Trans. Ind. Appl.*, vol. 53, no. 5, pp. 4695–4707, Sep./Oct. 2017.
[24] M. Wang et al., "Module power balance control strategy for three-phase cascaded H-bridge PV inverter under unbalanced grid voltage condition," *IEEE J. Emerg. Sel. Topics Power Electron.*, vol. 9, no. 5, pp. 5657–5671, Oct. 2021.
[25] R. P. Aguilera et al., "Predictive control of cascaded H-bridge converters under unbalanced power generation," *IEEE Trans. Ind. Electron.*, vol. 64, no. 1, pp. 4–13, Jan. 2017.
[26] X. Zhang et al., "A grid-supporting strategy for cascaded H-bridge PV converter using VSG algorithm with modular active power reserve," *IEEE Trans. Ind. Electron.*, vol. 68, no. 1, pp. 186–197, Jan. 2021.
[27] P. Li, R. Dargaville, Y. Cao, D.-Y. Li, and J. Xia, "Storage aided system property enhancing and hybrid robust smoothing for large-scale PV systems," *IEEE Trans. Smart Grid*, vol. 8, no. 6, pp. 2871–2879, Nov. 2017.
[28] G. Wang, M. Ciobotaru, and V. G. Agelidis, "Power smoothing of large solar PV plant using hybrid energy storage," *IEEE Trans. Sustain. Energy*, vol. 5, no. 3, pp. 834–842, Jul. 2014.
[29] L. Zhang, Z. Zhang, J. Qin, D. Shi, and Z. Wang, "Design and performance evaluation of the modular multilevel converter (MMC)-based grid-tied PV-battery conversion system," in *Proc. IEEE Energy Convers. Congr. Expo.*, Portland, OR, USA, 2018, pp. 2649–2654.
[30] S. Nayak, A. Das, R. E. Torres-Olguin, S. D'Arco, and G. Guidi, "Battery energy support to cascaded H-bridge converter-fed large-scale PV system during unbalanced power generation," *IEEE Trans. Ind. Appl.*, vol. 58, no. 6, pp. 7479–7489, Nov./Dec. 2022.
[31] Z. Malekjamshidi and M. Jafari, "Comparative analysis of DC to AC conversion cells for application in PV-linked grid-connected modular multi-level cascaded converters," *IET Power Electron.*, vol. 13, no. 15, pp. 3360–3372, 2020.
[32] N. Naseem and H. Cha, "Quad-active-bridge converter with current balancing coupled inductor for SST application," *IEEE Trans. Power Electron.*, vol. 36, no. 11, pp. 12528–12539, Nov. 2021.
[33] "List of microgrid demonstration projects from National Energy Administration of China," Accessed: Jun. 22, 2023. [Online]. Available: http://zfxxgk.nea.gov.cn/auto87/201705/t20170511_2789.htm
[34] S. Morozumi, "Micro-grid demonstration projects in Japan," in *Proc. Power Convers. Conf.*, Nagoya, Japan, 2007, pp. 635–642.
[35] L. Mariam et al., "Microgrid: Architecture, policy and future trends," *Renewable Sustain. Energy Rev.*, vol. 64, pp. 477–489, 2016.
[36] N. W. A. Lidula and A. D. Rajapakse, "Microgrids research: A review of experimental microgrids and test systems," *Renewable Sustain. Energy Rev.*, vol. 15, no. 1, pp. 186–202, 2011.
[37] L. Zheng, R. P. Kandula, and D. Divan, "Current-source solid-state DC transformer integrating LVDC microgrid, energy storage, and renewable energy into MVDC grid," *IEEE Trans. Power Electron.*, vol. 37, no. 1, pp. 1044–1058, Jan. 2022.
[38] H. Zhao, M. Hong, W. Lin, and K. A. Loparo, "Voltage and frequency regulation of microgrid with battery energy storage systems," *IEEE Trans. Smart Grid*, vol. 10, no. 1, pp. 414–424, Jan. 2019.

Xiaofeng Sun (Member, IEEE) received the B.S. degree in electrical engineering from Northeast Heavy Machinery Institute, Qiqihar, China, in 1993, and the M.S. and Ph.D. degrees in power electronics from Yanshan University, Qinhuangdao, China, in 1999 and 2005, respectively.

From 2003 to 2007, he was an Associate Professor with Yanshan University, where he has been a Professor since 2008. He is also the Director of the Key Laboratory of Power Electronics for Energy Conservation and Motor Drive of Hebei Province, Yanshan University. He has authored or coauthored more than 200 transactions and conference papers. His research interests include dc–dc converters, multiple-input converters, hybrid electric vehicles, microgrids, and power quality control.

Xinlei Liu received the B.S. degree in electrical engineering from Hefei Institute of City, Hefei, China, in 2021. He is currently working toward the M.S. degree in electrical engineering with Yanshan University, Qinhuangdao, China.

His research interests include modular multilevel converter and solid-state transformer insulation.

Jiaxun Teng (Student Member, IEEE) received the B.S. degree in electrical engineering from Harbin Institute of Technology, Weihai, China, in 2017, and the M.S. degree in power electronics, in 2021, from Yanshan University, Qinhuangdao, China, where he is currently working toward the Ph.D. degree in artificial intelligence.

Since 2021, he has been with the Key Laboratory of Power Electronics for Energy Conservation and Motor Drive of Hebei Province, Yanshan University. He has authored/coauthored more than 20 transactions and journal papers since 2021. His research interests include circuit topology, analysis and control of modular multilevel converter-based medium- and high-voltage direct current systems, multibus multiport energy router, medium-voltage motor drive, and power electronics transformer.

Ying Zhang received the B.S. and M.S. degrees in electrical engineering and power electronics and power drives, in 2005 and 2009, respectively, from Yanshan University, Qinhuangdao, China, where she is currently working toward the Ph.D. degree in artificial intelligence.

Her research interests include dc–dc converters and power quality.

Lei Qi received the B.S. and M.S. degrees in electrical engineering in 2014 and 2017, respectively, from Yanshan University, Qinhuangdao, China, where he is currently working toward the Ph.D. degree in power electronics.

He was a Lecturer with Yanshan University. His research interests include the energy management, nanogrids, and stability analysis.

Wei Zhao received the B.S. and M.S. degrees in electrical engineering and power electronics and power drives and the Ph.D. degree in power electronics from Yanshan University, Qinhuangdao, China, in 2006, 2009, and 2020, respectively.

His research interests include the stability analysis of microgrid and power quality.

Xin Li received the B.Eng. degree in computer software and applications from Northeast Heavy Machinery College, Yanshan University, Qinhuangdao, China, in 1992, and the M.Eng. degree in measurement technique and automation equipment and the Ph.D. degree in measurement technology and instruments from Yanshan University, in 2002 and 2008, respectively.

Her research interests include power electronics, intelligent information processing, bioinformatics, and biomedical instruments.